Master Thesis

Atomic Scale Friction and Contact Dynamics: Simulation and Experiment

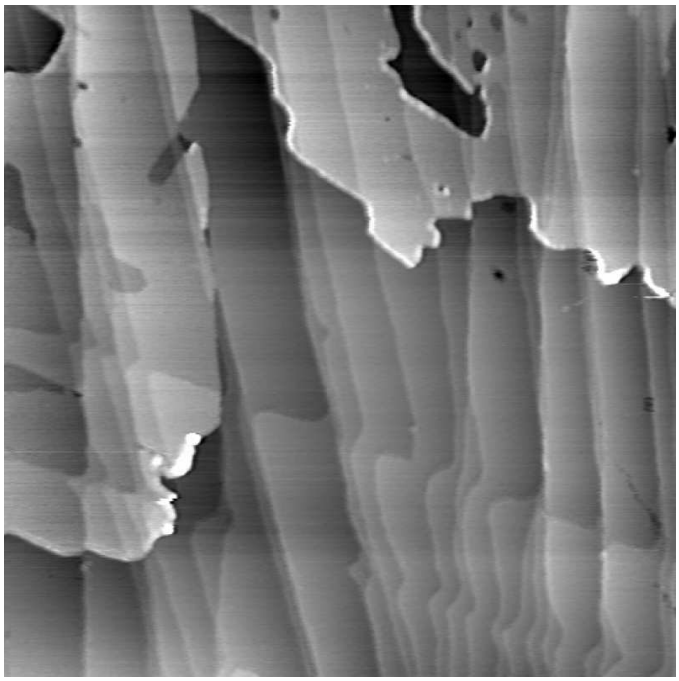

Raphael Roth

November 2007 - June 2008

Supervisors:
Dr. Thilo Galtzel
Dr. Enrico Gnecco
Prof. Dr. Ernst Meyer

Departement of Physics
University of Basel

Abstract

Although the study of friction between solid bodies has been an crucial field in physics for hundreds of years, controlling friction and wear has become more and more inevitable nowadays. Since the scale of mechanical devices shrank drastically in the last 50 years, an alternative to liquid lubricants must be found. Because of the large surface to volume ratio, the adhesion force is too strong for liquid lubricants [1]. The search of ways to understand and control friction has been the main effort in the field of Nanotribology in the last years, especially here at the University of Basel. In terms of contact Atomic Force Microscopey (AFM), a tiny cantilever acts as a probe for frictional and normal forces. With this work, the study of frictional behavior is carried on from well defined surfaces like alkali halide single crystals to a little bit more complex system: ultra thin films of NaCl on Cu(111). This system has the advantage (besides the study of thin film growth) of having two different materials on it that can be investigated with almost the same cantilever-tip conditions. The regime of ultra-low friction by actuation of the contact that has recently been discovered [2] has its first application in terms of superlubric imaging which drastic reduction of wear on these very weak bound systems.

As a second part of this work, theoretical considerations and simulations have been done to obtain a better understanding of the most fundamental mechanisms of sliding friction between atomic flat surfaces. In the framework of the Tomlinson model, temperature and piezo-actuation dependence of the friction has been investigated. With an extended Tomlinson model, the effect of actuating the cantilever during imaging has been be studied in one and two dimensions.

Contents

List of Abbreviations

A	Crosssection of the cantilever
AFM	Atomic force microscope
AFAM	Atomic force accoutic microscope
A_R	Real area of contact between to solids
a	Lattice constant
a_C	Radius of the contact area
α	Magnitude of actuation in dynamic Tomlinson model
β	Dimensionless parameter in the steepest descent algorithm
$c_{0,1,2}$	Correlation parameters in Ermak's algorithm
Cu	Copper
δt	Timestep
Δf	Frequency shift
E	Young's modulus
$E*$	Effective Young's modulus
E_0	Corrugation amplitude
ϵ	Angle between cantilever and sample
η	Dimensionless parameter in Tomlinson model
η_{min}	Minimum of η in case of actuation
η_{max}	Maximum of η in case of actuation
F_C	Contact force between tip and sample
F_L	Friction force in scanning-direction
$F_{L,max}$	Maximal friction force in scanning-direction
F_N	Externally applied normal force on the cantilever (=load)
$f_{n,free}$	Resonance frequency of the n'the eigenmode of the free cantilever
f_0	First normal resonance frequency $f_{1,free}$
$f_{n,cont}$	Resonance frequency of the n'the eigenmode of the cantilever in contact
F_{ts}	Tip-sample interaction forces
FFM	Friction force microscope
G	Shear modulus
$G*$	Effective shear modulus
$\vec{g}(f)$	Gradient of a function f
Γ	Damping rate

γ	Damping
γ_c	Critical damping
h	Height of the tip
HOPG	Highly orderd pyrolytic graphite
I	Area moment of inertia
k_{exp}	Experimental lateral contact stiffness
k_{eff}	Effective lateral contact stiffness
k_N	Normal stiffness of the cantilever
k_T	Torsional stiffness of the cantilever
$k*$	Normal contact stiffness
$k_{n,cont}$	Wavenumber of the cantilever in contact vibrating in the n'th eigenmode
$k_{n,free}$	Wavenumber of the free cantilever vibrating in the n'th eigenmode
κ	Lateral contact stiffness
k_x	Stiffness of the system in x-direction in the Tomlinson model
k_y	Stiffness of the system in y-direction in the Tomlinson model
KPFM	Kelvin probe force microscope
L	Total lenght of the cantilever
L'	Lenght from the center of the tip to the end of the cantilever
L_1	Lenght from the chip to the tip
M	Indentation modulus
$m*$	Effective mass of the cantilever
m_{tip}	Mass of tip
μ	Coefficient of friction
ML	Monolayer
ν	Poisson's ratio
NaCl	Natrium-chloride
nc-AFM	Non-contact AFM
ω	Angular frequency
p	Pressure
PLL	Phase-locked loop
R	Radius of the tip-apex
$\vec{r}$	Spatial vector (x,y,z)
$\vec{r}^G$	Gaussian distributed random displacements
ρ	Mass density
σ	Shear strenght
SFM	Scanning force microscope
SPM	Scanning probe microscope
STM	Scanning tunnel microscope

T	Temperature
t	Thickness of the cantilever
τ	Strain
$v_{1,2}$	Model parameters of the interaction potential
V_{int}	Tip-sample interaction potential
$\vec{v}^G$	Gaussian distributed random velocities
w	Width of the cantilever
$\xi(t)$	Noise (random numbers)
x_{tip}, y_{tip}	Spatial coordinates of the tip position
x_{sup}, y_{sup}	Spatial coordinates of the cantilever-support position
$y(x,t)$	Deflection of the cantilever (shape-function)

1 Principles of SPM

The atomic force microscope (AFM) (or scanning force microscope (SFM)) is a high-resolution type of a scanning probe microscope (SPM), with a demonstrated resolution of fractions of a nanometer. This is approximately 1000 times smaller compared to resolution of light microscopes, which are strongly limited by diffraction. The principle of an AFM is quite simple: While sliding over a sample (substrate), the response (deflection) of a thin beam (called cantilever), with a tiny probing-tip attached at one end, is used as a force-sensor (force probe). In a way this technique is similar to a phonograph, whose needle slides over the disc probing its roughness. A schematic setup of a typical AFM is shown in fig. 4.2(a) Picture of the combined home-built AFM/STM. In order to improve visibility, this photo was taken when the AFM was outside the UHV-chamber. (b) Schematic view of the microscope with beam-deflection method, taken from [24].figure.caption.25. Another variety of SPM, the scanning tunneling microscope (STM), was developed by Gerd Binnig and Heinrich Rohrer in the early 1980s, a development that earned them the Nobel Prize for physics in 1986. In contrast to an AFM, an STM uses the tunnel effect of electrons, which is used to probe conductive surfaces by a metal (tungsten or wolfram) tip which measures the exponential distance dependent tunneling current. For the first time, the individual surface atoms of flat samples could be made visible in real space (e.g. for silicon or highly ordered pyrolytic graphite (HOPG)).

Binnig, Quate and Gerber then invented the first AFM in 1986 [3], which used a STM to measure the spatial deflection of the cantilever. Depending on the situation, forces that are measured in AFM include mechanical contact forces, Van der Waals forces, capillary forces, chemical bonding forces, electrostatic forces, magnetic forces, Casimir forces and solvation forces. Therefore, the results from AFM experiments have to be analyzed carefully, since one not only means the "topography" in a common sense (the word "topography" becomes unprecise at this point).

In principle, there are also two methods to force a relative movement between the cantilever and the surface. Either, the cantilever is moved over the fixed sample, or the sample is moved and the cantilever is fixed. The latter has the advantage of suppressing additional vibrations of the microscope that leads to noise. In each case, the movement of the parts is realized with piezoelectric materials (also called piezos) that allows very accurate length adjustments by applying a certain voltage. If one wants to move the cantilever, it is common to use three separate x-,y- and z-piezos, while for moving the sample, it is easier to use a piezo-tube.

One way to image a sample is to keep the z-piezo at a constant height while taking the "force" (see above) as imaging signal. The other way would be to use the "force" as a input for a feedback loop, which adjust the z-piezo in such a way that the force keeps constant. The constant-height mode is only recommendable if scanning very flat surfaces, since large topographical features could possible destroy the tip.

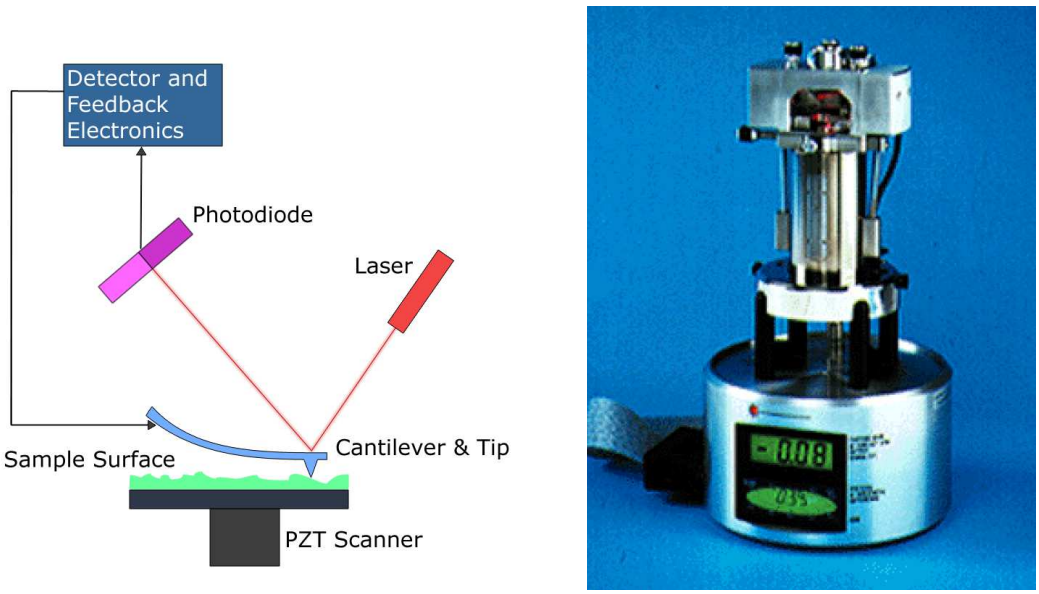

(a) (b)

Figure 1.1: *(a) The most common setup of an atomic force microscope with beam deflection method. (taken from [4]) (b) A commercial available AFM operated in air (Veeco).*

Nowadays, there exist mainly two techniques to quantitatively measure the cantilever deflection. One method is to detect the displacement via a interferometer, the other method is to position a laser spot on the cantilever and then measure its deflection on a 2- or 4-quadrant photodiode [5]. The first technique has the advantage of a more accurate detection of spatial displacements of the cantilever, since angular deformations are not detected (they are indeed difficult to take into account in the calibration). On the other hand, the latter technique allows to track simultaneously the lateral deflection (twist) of the cantilever, which is crucial for friction measurements.

The first microscopes have been operated in a static mode, where only the static deflection of the cantilever was used as a force signal. Although it was possible to image the atomic structure of the sample, one never obtained real atomic resolution in a sense of imaging single atomic features (like atomic defects). It took another 9 years before Giessible presented a dynamic imaging technique with higher resolution capabilities, the non-contact AFM (nc-AFM). A good overview of the history of SPM and recent developments is given in [6]. The main operating modes are now described more precisely, even though it is not possible to go into details within this work, since a lot of imaging techniques have been developed in the last 10 years.

1.1 Contact Mode

The easiest operation mode of an AFM is to move the cantilever across the surface, taking the static vertical deflection signal of the photodiode as force signal. As the cantilever can be approximated well with an ideal spring with a normal spring constant k_N of about 1 N/m, the normal force F_N is proportional to the displacement Δz (Hook's law).

$$F_N = k_N \Delta z \quad . \tag{1.1}$$

If a feedback-loop is used, the vertical deflection is kept at a constant value, while the controller-signal then contains the topographic information. As a modification of the contact AFM, it is common to interpret the horizontal deflection signal as a measure for frictional forces, since torsion of a angle β of the cantilever is also proportional to the lateral force acting on the tip:

$$F_L = k_T \Delta \beta \quad . \tag{1.2}$$

Under these conditions, one speaks of a friction force microscope (FFM). Since lateral and normal deflection can be tracked simultaneously with a 4-quadrant photodiode, it is a powerful tool to characterize the sample without further effort or experimental needs. One of the advantages of the contact mode is the dominance of short-range forces like repulsive ionic forces, since the tip is very close to the surface. As mentioned above, the disadvantages of this operation mode are the limitations in resolution and due to direct contact between tip and sample, the surface wear may sets in. More experimental details concerning contact-AFM and FFM can be found in section 4Experimental Setupsection.4.

1.2 Dynamic Mode

In the nc-AFM, the cantilever is excited at its resonance frequency f_0 by an actuator or an ac-voltage between tip and sample. Now, there are two fundamental techniques to sense forces with the oscillating cantilever: In amplitude-modulation (AM)-AFM [7], the cantilever is driven at a frequency near to f_0 and change of the amplitude due to interaction forces is taken as a feedback signal. But since the quality factor (Q-factor) of the cantilever (especially in vacuum) are very high, the AM-AFM mode is only used in air. This was overcome by the invention of the frequency-modulation (FM)-AFM [8], where the change of the eigenfrequency of the cantilever is taken as a signal. Since f_0 is normally > 100 kHz, this detection mode is very fast with a response timescale of $\approx 1/f_0$. The connection between frequency shift and (conservative!) tip-sample interaction forces F_{ts} is given by [9]:

$$\Delta f = -\frac{f_0}{kA^2}\langle F_{ts} q' \rangle \approx -\frac{f_0}{2k}\frac{\partial F_{ts}}{\partial z} \quad , \tag{1.3}$$

where, $\langle \quad \rangle$ denotes the time average over one oscillation cycle and q' the deflection of the cantilever and z is the distance between tip and sample. The amplitude A

is in the range of 1-15 nm, depending on the circumstances. The interaction forces contain short-range forces (e.g. chemical forces) as well as long range forces (e.g. van-der-Waals forces), both of them are always attractive. In FM-AFM, one can use a phase-locked-loop (PLL, see 4.3Electronicssubsection.4.3 for more details), which is able to detect and excite the cantilever typically first at its resonance frequency $f_0 + \Delta f$. Therefore, the frequency-shift can be used as a feedback signal which controls the z-piezo dynamically. The quantitative understanding of the frequency-shift is not straight-forward, since many forces contribute differently to F_{ts}. Especially long range forces are not advantageous for obtaining a maximum resolution.

1.3 Other Operation Modes

As mentioned above, there exist many variations of these two operation modes. First of all, one can obtain additional informations if the cantilever is kept at a certain place on the sample ($x, y = \text{const}$) and only z is changed. The recorded signal as a function of the tip-ample separation z ("z-spectroscopy") delivers information about the system that can not be obtained during regular scanning. When recording, the resulting curve is called a "force-distance-curve", which is necessary to calibrate the sensitivity of the setup (see 4.5Calibrationsubsection.4.5). Such a curve is sketched in fig. 1.2(a) A force-distance-curve taken in contact AFM on a KBr sample. The blue one is the approach curve, while the red one is the retract curve. One can clearly see the point where the tip snaps into contact, then the linear part represents k_N or the sensitivity of the setup. While retracting, strong pulling forces have to be applied to the cantilever to overcome the omnipresent adhesion forces between tip and sample. (b) Z-spectroscopy (only approach) in non-contact mode over a HOPG sample. If the tip oscillates far enough over the surface, Δf is almost linear (attractive regime), while the interaction changes drastically when entering the repulsive regime.figure.caption.5.

In nc-AFM, the z-spectroscopy is a widely used tool to probe the tip-sample potential. When sweeping over a sufficient large z-range, one can clearly identify a Leorand-Jones like potential with the typical turnaround-point when entering the repulsive regime. Other variation of AFM [10] include: Tapping mode [11], Kelvin probe force-microscopy (KPFM) [12], magnetic force microscopy (MFM) [13], atomic force acoustic microscopy (AFAM) [14] and many more.

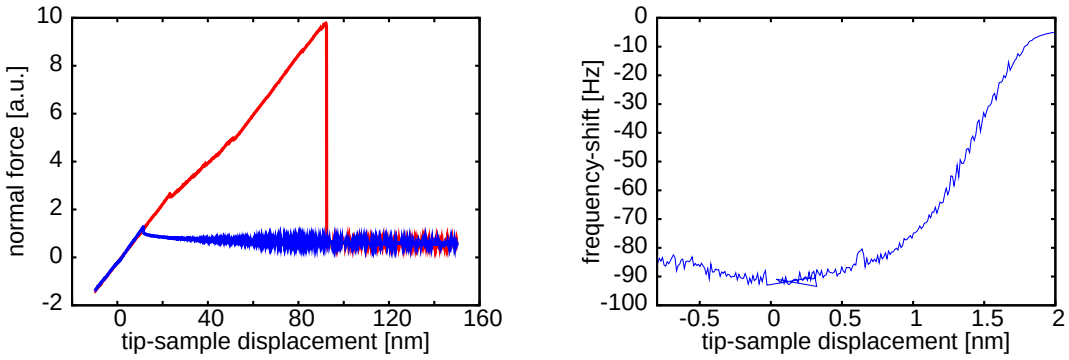

(a) (b)

Figure 1.2: *(a) A force-distance-curve taken in contact AFM on a KBr sample. The blue one is the approach curve, while the red one is the retract curve. One can clearly see the point where the tip snaps into contact, then the linear part represents k_N or the sensitivity of the setup. While retracting, strong pulling forces have to be applied to the cantilever to overcome the omnipresent adhesion forces between tip and sample. (b) Z-spectroscopy (only approach) in non-contact mode over a HOPG sample. If the tip oscillates far enough over the surface, Δf is almost linear (attractive regime), while the interaction changes drastically when entering the repulsive regime.*

2 Nanotribology

2.1 Macroscopic Friction

Friction has been studied for several centuries and remarkable scientists established macroscopic friction laws valid up to now. Leonardo da Vinci can be named the father of modern tribology (Greek tribos: rubbing). To the pioneers in tribology one counts besides Leonardo da Vinci also Guillaume Amontons, John Theophilius Desanguliers, Leonard Euler, and Charles-Augustin Coulomb. These pioneers brought tribology to a standard, and their findings still apply to many engineering problems today. All of these remarkable scientist collected a big repository of empirical knowledge of the phenomenology of sliding friction. The three most important friction-laws for (dry friction) determined by these physicist are namely:

Leonardo's Law
Friction is independent of the apparent area of contact

Law of Amontons and Euler
The friction force F_L (="Friction") is proportional to the applied load. The ratio $\mu = F_{L,max}/F_N$ is called coefficient of friction, where $F_{L,max}$ is the maximal tangential force before sliding begins, and F_N denotes the applied normal force (=load). It is larger for static friction than for kinetic friction

$$F_L = \mu F_N \quad . \tag{2.1}$$

Coulombs Law
Kinetic friction is independent of the velocity.

These three fundamental laws of friction, which are based on macroscopic experiments, are still not fully understood in terms of a microscopic theory. In fact, improvements in the experimental techniques, which allows us nowadays to study friction in terms of single atomic asperities, show that these laws loose their validity. In the end of the 19^{th} century, Reynolds recognized the hydrodynamic nature of liquid lubricants, and introduced a theory of fluid-film lubrication. Still today, Reynolds steady state equation of fluid-film lubrication is valid for hydrodynamic lubrication of thick films. In the 20^{th} century both dry friction and lubricated friction theories were further developed. The adhesion concept of friction, already proposed by Desanguliers, was applied with great success by Bowden and Tabor to metal-metal interfaces [15]. Adhesion was related to the force required to separate two bodies in contact. In their model the concept of the real contact area was introduced. The real area of contact consist of a large number of small contact regions, where atomic contacts occurs. A main result of Bowden and Tabor was

$$F_L = \sigma A_R = \frac{\sigma}{p_m *} F_N \quad , \tag{2.2}$$

where A_R is the real contact area, σ the shear strength and p_m^* the yield pressure of the asperity.

So, after leaving the pictures of infinite hard body models could be improved well by introducing plastic deformation of materials. In this picture, a lot of experiments could be explained in a more fundamental way, but also it made the analytical calculations more complicated. A lot of work has been done by Hertz, who developed a theory of (point) contact within elastic theory [16]. One of the most striking results of his theory was the relation $F_L \propto F_N^{2/3}$, which is in contradiction to Amontons' law. But this contradiction could soon be solved by Archard, who understood to apply single asperity mechanics on macroscopic bodies [17]. A possible application of this theories on the three fundamental laws may be as follows:

Leonardo's Law: The real (microscopic) area of contact is invariant of the apparent (macroscopic) area of contact, it depends only on the static load.

Law of Amontons and Euler: As a consequence from above, the real area of contact, which is crucial for the friction force, is proportional to the load.

Coulombs Law: Is a consequence of the elastic properties of the contact area

[18].

There were of course many other approaches and extensions to the theories mentioned above, namely the models presented by Johnson-Kendall-Roberts (JKR), Derjaguin-Muller-Toporov (DMT), Bradley and Maugis Dugdale. In principle, each of these models describes very well a narrow regime of applications (e.g. depending on the involved materials). A more sophisticated approach was done by Greendwood and Williams (1966), which investigated a surface with random distributed asperity heights [19]. They could again show that $F_L = \sigma A_R \propto \sigma F_N$. Also, other height distributions have been considered, e.g. exponential and Gaussian distributed asperities. The great success of the Greenwood and Williamson theory was due to the explanation of Amonton's law without the (unphysical) assumption, that every deformation between the asperities is plastic. However, the experimental determination of the number and height distribution of the asperities were the main problem of this theory. Experimental setups for non-atomic friction measurements included at that time classical tribometers and surface force apparatus (SFA) [20].

As it is the case in most scientific research areas, it is necessary to understand a phenomena in a microscopic way. The concept of considering single asperities was a major step in the understanding of friction, since macroscopic law's could be understood by considering an ensemble of single asperities. And this is now the point where single atoms takes the role of the asperities.

2.2 Friction at the Atomic Scale

As a consequence from the historical overview, it should nowadays be the main goal to understand friction at an atomic point of view. One of the evidences for single atomic asperities was the observation of stick-slip patterns on graphite sheets [21] using modern friction microscopes. From the length scale of the typical sawtooth-pattern it was obvious that the underlying mechanism must be a "small" asperity sliding over the energy corrugation potential of the underlying substrate. A very simple but still powerful model to explain and study friction at the atomic scale is the Tomlinson model [22].

2.2.1 Tomlinson Model

The model of molecular friction proposed by British physicist G.A. Tomlinson [22] describes and explains the occurrence of unstable equilibrium positions of atoms in a conservative potential. All the following expressions are given for one dimension, but they also hold true for a two-dimensional system (see section 3Simulationssection.3). The simplest case of this model consists only of one asperity attached to a spring. Applied to the principle of a FFM, the tip of the cantilever, assumed to be infinitesimal small, slides over a rigid surface, represented by a so called adiabatic potential or tip-sample potential $V_{int}(x)$. In a first approx-

imation, this potential is well represented by a sinusoidal-shaped function. On the other hand, the deformation of the (cantilever-) spring with spring constant k (k_x and k_y respectively, when working in two dimensions) gives rise to a energy $\frac{1}{2}k(x_{tip}-x_{sup})^2$, where x_{tip} denotes the position of the asperity in the surface, while $x_{sup} = v_{sup} \cdot t$ is the position of the spring-support (here: the cantilever-support), respectively. Therefore the system is characterized by its total energy :

$$E_{tot} = \frac{1}{2}k(x_{tip} - x_{sup})^2 + V_{int}(x) \quad . \tag{2.3}$$

It is important to see that the first term in eq. (2.3Tomlinson Modelequation.2.3) depends on the relative distance between tip and support, while the second term only depends on the tip position. If we also introduce a mass of the tip m_{tip} and a damping rate $\Gamma = \gamma/m_{tip}$ (while γ is the damping) , we can immediately write down the equation of motion for the potential in eq. (2.3Tomlinson Modelequation.2.3):

$$\frac{d^2x_{tip}}{dt^2} + \Gamma\frac{dx_{tip}}{dt} + \omega(x_{tip} - x_{sup})^2 = \frac{\partial V_{int}}{\partial x_{tip}} \qquad , \tag{2.4}$$

with $\omega_{tip} = \sqrt{k/m_{tip}}$. Of course, the interaction potential has to be periodic in space (with periodicity a), which implies $V_{int}(x) = V_{int}(x + a)$. In one dimension, one often chooses

$$V_{int}(x) = -\frac{E_0}{2}cos(\frac{2\pi}{a}x_{tip}) \quad . \tag{2.5}$$

Here, E_0 denotes the amplitude of the energy corrugation, which is normally around 1eV.

With this dependencies, we can easy understand the mechanism of atomic stick-slip motion. In fig. 2.1Representation of the stick-slip motion within the framework of the Tomlinson model. The cantilever is stuck in a minimum as long as the energy stored in the spring is smaller than the energy needed to overcome the barrier to the next minimum.figure.caption.9 the parabola in the energy-space arising form the deformation of the spring is illustrated. Because of this shift, the tip, which is stuck in a local minima (separated from the next mini by an barrier energy ΔE, can suddenly jump in the next minima as soon as the energy of the spring exhibits a certain value. One has to mention that for T=0 K, the jump only occurs if ΔE vanishes. However, for finite temperatures, thermal activation may allows the tip to overcome a non-zero barrier height (Prandtl-Tomlinson-Model).

If one defines the friction force as

$$F_L = -k(x_{tip} - x_{sup}) \quad , \tag{2.6}$$

then the friction force and the tip-position as a function of the support position looks like in fig 2.2Mechanism of stick-slip motion sketched in energy-space (a) and in spatial-space (b). For a low value of E_0 (or low k) one obtains a smooth pattern (c)figure.caption.10 (b). By analyzing the conditions for the position of

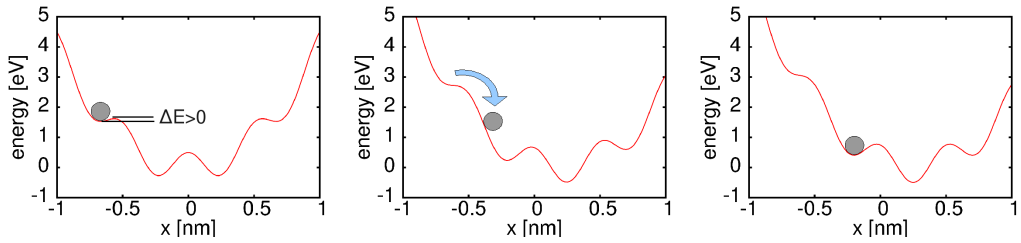

Figure 2.1: *Representation of the stick-slip motion within the framework of the Tomlinson model. The cantilever is stuck in a minimum as long as the energy stored in the spring is smaller than the energy needed to overcome the barrier to the next minimum.*

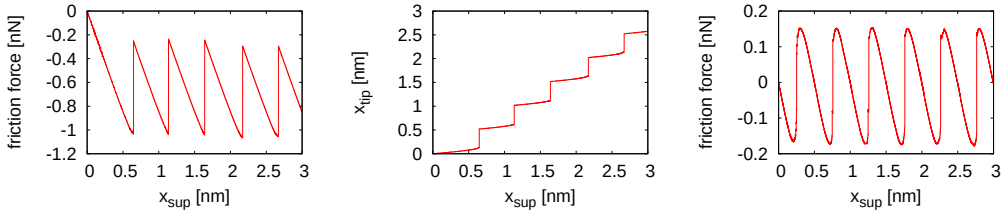

Figure 2.2: *Mechanism of stick-slip motion sketched in energy-space (a) and in spatial-space (b). For a low value of E_0 (or low k) one obtains a smooth pattern (c)*

the tip ($\partial V_{int}(x)/\partial x_{tip}$) one can rewrite (2.6Tomlinson Modelequation.2.6) by using (2.5Tomlinson Modelequation.2.5):

$$F_L = -\frac{\pi E_0}{a} sin(\frac{2\pi}{a} x_{tip}) \quad . \tag{2.7}$$

For the maximum value of F_L (at x=$a/4$) we therefore get $F_{L,max} = \frac{\pi E_0}{a}$.

For a cantilever movement from $x_{start} = 0$ to $x_{end} > 0$ ('forward scan') the friction force decreases linearly ('sticking-part') until the tip jumps to the next minima at $F_{L,max}$, then it repeats again until a regular sawtooth shaped curve is produced. In the spatial-space, the mechanism is as follows: x_{tip} is constant as a function of x_{sup} until the tip jumps, then $x_{tip} = x_{tip} + a$. Therefore the curve is characterized by plateaus with a length of a.

An important parameter to characterize the system is given by [23]

$$\eta = \frac{2\pi^2 E_0}{k a^2} \quad . \tag{2.8}$$

This parameter represents the fraction between the potential energy the spring-energy. For $\eta > 1$ one gets the normal stick-slip motion as sketched in fig. 2.2Mechanism of stick-slip motion sketched in energy-space (a) and in spatial-space (b). For a low value of E_0 (or low k) one obtains a smooth pattern (c)figure.caption.10 (a), while for $\eta < 1$ the x_{sup} vs. F_L curve becomes smooth and the average friction

force becomes negligible [23]. The curve then represents a 'stretched' shape of the interaction potential as shown in fig. 2.2Mechanism of stick-slip motion sketched in energy-space (a) and in spatial-space (b). For a low value of E_0 (or low k) one obtains a smooth pattern (c)figure.caption.10 (c).

The energy dissipated during this process is simply given by

$$E_{diss} = \bar{F_L}(x_{start} - x_{end}) \quad , \tag{2.9}$$

where $\bar{F_L} = \frac{1}{t}\int F_L(t')dt'$ is the time averaged friction force or residual friction. In experiments, one clearly recognizes the energy dissipation as a finite area between forward and backward-scan (hysteresis-loop). The cause of this energy-loss is discussed in section 2.2.2Mechanisms of Energy Dissipationsubsubsection.2.2.2. Of course, one can think of many variations of extending this basic model. For example, one could consider more than one spring or a tip consisting of of many minitips [24]. It is also possible to modify the corrugation amplitude $E_0 = E_0(t, ...)$ to simulate an actuated cantilever or a buried interface [25]. The case of a time-dependent E_0=0 became especially important, since this allows to model the state of dynamic superlubricity [2, 24].

Thermal Activation

An alternative way to model the Tomlinson mechanism is to describe this process as a forced Brownian motion. As the energy barrier ΔE of the tip sliding over single atoms is small, the effect of thermal vibrations with an energy in the order of $k_B T$, where k_B is the Boltzmann constant, should not be neglected. The basic idea in this so-called "Prandtl-Tomlinson"-model is to include a Gaussian distributed random force $\xi(t)$ which satisfies the fluctuation-dissipation-theorem $\langle \xi(t)\xi(t')\rangle = 2m_{tip}\gamma_{tip}k_B T\delta(t-t')$. The system is then described by the Langevin-equation [26]:

$$\frac{d^2 x_{tip}}{dt^2}m_{tip} + \gamma\frac{dx_{tip}}{dt} + \frac{\partial V_{int}}{\partial x_{tip}} = \xi(t) \qquad . \tag{2.10}$$

A method to solve this equation is described in section 3.2.2Langevin Equationsubsubsection.3.2.2, where Ermak's algorithm is used to numerically solve eq. (2.10Thermal Activationequation.2.10). A detailed description of this mechanism applied especially to SPM is given in [27]. The authors point out the importance of dissipative effects due to deformations of the tip and the concomitant thermal fluctuations. Additionally, thermal baths both for substrate and tip should be taken into account.

Dynamic Extension of the Tomlinson Model

One possibility to understand the influence of an actuation of the cantilever is to modulate the interaction-potential amplitude E_0 in eq. (2.5Tomlinson Modelequation.2.5) in time with a frequency f and a phase ϕ:

$$E(t) = E_0(1 + \alpha sin(2\pi ft + \phi)) \quad . \tag{2.11}$$

This ansatz seems plausible, since a vibrating tip is equivalent to a periodic change in the tip-sample-interaction. In this notation, α denotes the normalized actuation-amplitude in units of E_0. Due to this modification, eq. (2.8Tomlinson Modelequation.2.8) is not constant anymore. Instead, there are now two extreme values:

$$\eta_{max} = \frac{2\pi^2 E_0}{ka^2} \tag{2.12}$$

$$\eta_{min} = \frac{2\pi^2 E_0(1-\alpha)}{ka^2} \tag{2.13}$$

It has been shown [24] that in the case of an actuation, η has to be replaced by η_{min}, since jumps occure when $E_0(t)$ becomes minimal. Then again, if $\eta_{min} < 1$, the transition from stick-slip motion to a smooth sliding can be reproduced (see 3.3Resultssubsection.3.3).

2.2.2 Mechanisms of Energy Dissipation

One of the central questions addressed in atomic friction studies concerns the dissipation of energy (which is allways the case!). In the typical atomic stick-slip motion, the motion of the cantilever is adiabatic, except for the jump-phase. Within these very small timescale (few μs, see ref. [24] for details) when the slip takes place, the tip-sample interaction becomes non-adiabatic and as a consequence, inner degrees of freedom both of the tip and the sample can be excited. The origin of dissipation in friction are therefore related to phonon excitations, electronic excitations, and irreversible changes of the surface (wear). The latter can be excluded in experiments where the atomic structure of a certain surface area can be repeatedly imaged. Nowadays, it is believed that phonon excitations contribute most to energy dissipation. Many models have been proposed to investigate such mechanism: Independent Oscillator (IO) model, Frenkel-Kontorova (FK) model, Frenkel-Kontorova-Tomlinson (FKT) model. But still, it is not yet clear how energy dissipation works in detail, since a experimental approach is difficult.

The energy dissipated in one slip is in the range of 1-4 eV [28], hence much smaller than the energy of typical ionic bonds. With usual scan-speeds of ≈ 10 nm/s, the mean power loss is approximately $\bar{P} \approx 10^{-16}$ W.

2.2.3 Model of the Contact

Hertzian Contact Model

One of the problems when measuring with SPM is the lack of knowledge how the tip-sample contact looks like. Therefore, it is difficult to determine the size of the tip and hence the contact-area between the tip-apex and the substrate (an estimation is given in section 5.4.3Models to Estimate the Contact Stiffnesssubsubsection.5.4.3).

As mentioned in above, Hertz developed in 1880 a model based on continuum mechanics (plastic deformation) [29, 30]. The Hertzian contact model investigates the interaction of a sphere with radius R which is pressed on a flat surface with the contact force F_C, which contains both the normal force F_N and the attractive tip-sample forces F_{ts}. Because of plastic deformations, a contact region with radius a_C is created, as sketched in fig. 2.3A Hertzian contact. Due to plastic deformation, a sphere with radius R which acts on a surface with the normal force F_C results in a finite contact region with radius a_C (taken from [31]figure.caption.14.

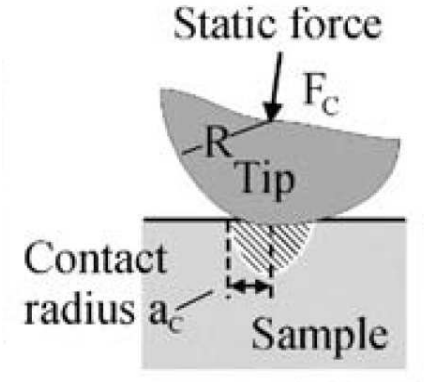

Figure 2.3: *A Hertzian contact. Due to plastic deformation, a sphere with radius R which acts on a surface with the normal force F_C results in a finite contact region with radius a_C (taken from [31]*

The radius of the contact region then reads

$$a_C = \sqrt[3]{\frac{3RF_C}{4E^*}} \quad , \tag{2.14}$$

with E^* being the reduced Young's modulus for the tip and the sample:

$$\frac{1}{E^*} = \frac{1-\nu_{tip}^2}{E_{tip}} + \frac{1-\nu_{sample}^2}{E_{sample}} \tag{2.15}$$

$$\frac{1}{E^*} = \frac{1}{M_{tip}} + \frac{1}{M_{sample}} \tag{2.16}$$

Here, ν denotes the Poisson's ratio (see appendix), which can for example be measured using contact-resonance AFM [32], and M the indentation modulus $M_i := \frac{E_i}{1-\nu_i}$. With these relations, the vertical (normal) stiffness of the contact k^* is given by the derivative of the force $F(z)$ at the equilibrium position z_e:

$$k^* = -\frac{\partial F(z)}{\partial z}\bigg|_{z=z_e} = 2a_C E^* \tag{2.17}$$

It can be shown that the normal pressure p distribution within the contact has a simple quadratic dependence on the radial distance from the center r:

$$p(r) \propto \sqrt{1 - \frac{r^2}{a_C^2}} \tag{2.18}$$

The above relations are valid only for forces acting perpendicular to the surface. However, there exist also similar expressions for shear forces [33]. The lateral contact stiffness κ can be written in a similar form as eq. (2.19Hertzian Contact Modelequation.2.19):

$$\kappa = -\frac{\partial F(x)}{\partial x}\bigg|_{x=x_e} = 8 a_C G^* \quad , \tag{2.19}$$

while in the lateral case, G^* is the reduced shear modulus

$$\frac{1}{G^*} = \frac{2-\nu_{tip}^2}{G_{tip}} + \frac{2-\nu_{sample}^2}{G_{sample}} \quad . \tag{2.20}$$

For isotropic materials, the relation $G_i = \frac{1}{2}\frac{E_i}{1-\nu_i}$ holds true.

One difficulty within the Hertz model is the treatment of adhesive forces. In the contact force F_C they are implicit included, hence it would be wrong to assume that F_C is equal to the static force (load) applied externally in FFM experiments. Since adhesion forces may be bigger than the static force (normally $\approx$ 1-5 nN), it is essential to treat them as independent contributing forces. Adhesion can be treated most simply in the opposite limits of very short-range interactions (JKR-model) [34] and of infinite range interactions (DMT-model) [35].

Non-Continuum Contact Models

The model discussed above is true for continuous materials. But if the investigated system is of length scales comparable to atomic ones, continuum mechanics is not any more indisputable. In common contact-AFM, tip radii are in the order of 10 to 1000 nm, therefore a spherical apex is not always adequate. It has been found [36, 37] that the atomic scale roughness present on any tip made of discrete atoms is shown to have profound effects on the results. This approach, which is mainly only accessible via atomistic simulations, shows impressively, how different tip morphologies (bent, amorphous or stepped) affect stress distribution on the substrate, as can be seen in fig. 2.4The top row shows the central regions of bent, amorphous and stepped spherical tips. The second and third rows show the pressure distributions for these tips with non-adhesive and adhesive interactions, respectively. (taken from [37])figure.caption.16. Contact areas, local stresses, and the work of adhesion change by factors of two to four, the friction and the lateral stiffness vary by orders of magnitudes. A conclusion of these simulations is that contact areas and yield stresses will be underestimated by continuum theory and that friction and contact stiffness will be overestimated.

But as a lack of such time-consuming simulations, the Hertz model will still be used for everyday use for many physicists. It seems to be important to keep in mind the limits of such simplified models especially for very sharp tips!

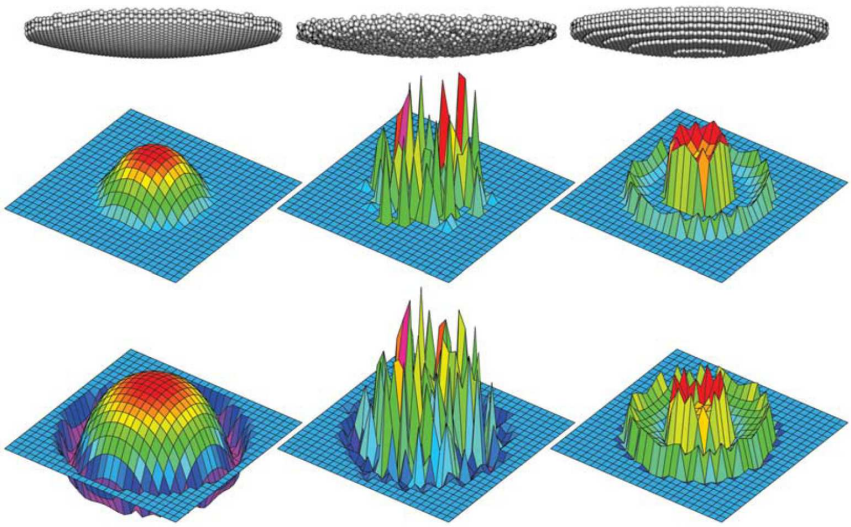

Figure 2.4: *The top row shows the central regions of bent, amorphous and stepped spherical tips. The second and third rows show the pressure distributions for these tips with non-adhesive and adhesive interactions, respectively. (taken from [37])*

3 Simulations

3.1 Motivation

In this chapter, two different methods are presented in order to numerically simulate the Tomlinson-mechanism. It is obvious that this model has strong limitations, e.g. compared to atomistic simulation. Instead of a realistic AFM tip with a finite size and elasticity, only one spring is used which touches the surface only at one point (one asperity). The corrugation potentail is infinite hard, meaning that all the surface elasticity is given by the spring. Therefore only the very basic behavior of friction can be reproduced, quantities like contact stiffness and the tip-sample potential have to be provide as input parameters. The theoretical background has already been discussed in section 2.2.1Tomlinson Modelsubsubsection.2.2.1. The implementation of such a simulation is very instructive, since one has to understand perfectly both the physics and the algorithms.

3.2 Numerical Methods

3.2.1 Energy Minimization

The easiest way to solve the Tomlinson problem is to have a look at the energy-space. This is of course possible for both one and two dimensions. The expression for the total energy is given in eq. (2.3Tomlinson Modelequation.2.3), it consists of a periodic potential which is a function of the tip coordinate, and a term arising from the deformation of the spring, which is a function of the tip and support position. The total energy in two dimensions is shown in fig 3.2(a) Total energy of spring and surface potential in two dimensions. (b) Potential map (eq. (3.4Energy Minimization 2Dequation.3.4) (with v_1=0, v_2=1) and a sketch of three different path of tip movement for different ratios of k_y/k_x (red: $k_y/k_x < 1$, green: $k_y/k_x \approx 1$, magenta: $k_y/k_x \gg 1$)figure.caption.18. We can use the fact that physical systems move in such a way, that their total energy is minimal. Therefore, a simple energy minimization algorithm can be used. In this case, the steepest-descent method with energy feedback was used as a tool to track the minimum energy position of a function given $f(\vec{r})$:

$$\vec{r}_{l+1} = \vec{r}_l - \beta \cdot \vec{g}(\vec{f}(\vec{r}_l)) \quad . \tag{3.1}$$

In our case, $\vec{r}$ is the (tip)-coordinate and $\vec{g}(\vec{f})$ denotes the gradient of the function f. This minimum position has to be found for each time step δt. This simple algorithm will converge to a minimum if β is sufficient small. To make the steepest descent method faster, the parameter β is adjusted in a following way: If the energy goes up, then we decrease β by a factor of $\frac{1}{2}$, if the energy goes down, we slightly increase β (e.g. by a factor of 1.05). Since the adiabatic potential has a quite simple trigonometric form, the derivatives can be calculated analytically, saving additional computer time. One has to be careful by choosing the time step

parameter and the initial value of β, especially in two dimensions. It is quite easy to set these parameters in such a way that the algorithm diverges at some points. Good values have been found to be δt=10^{-6}-10^{-7} s and $\beta \approx 10^{-4}$. The disadvantage of the energy-minimization method is the limitation to T=0 K, therefore no thermal effects can be studied.

3.2.2 Langevin Equation

The second method to implement the Tomlinson model is to solve the equation of motion. In contrast to the method discussed above, which is completely (quasi) static, the solution of the Langevin equation (2.10Thermal Activationequation.2.10) allows dynamics (e.g. tip oscillations, and thermal activated (mulitple-)jumps). Since this equation is a differential equation, it cannot be solved straight forward. One way to solve it is to implement the Ermak-algorithm [38]. In Ermak's approach, the equations of motions are integrated over a time interval δt under the assumption that the systematic forces $\vec{f}$(t) remain constant. The result is an algorithm based on stored positions $\vec{r}$, velocities $\vec{v}$ and accelerations $\vec{a}$:

$$\vec{r}(t+\delta t) = \vec{r}(t) + c_1 \delta t \vec{v}(t) + c_2 \delta t^2 \vec{a}(t) + \delta \vec{r}^G \quad , \tag{3.2}$$

$$\vec{v}(t+\delta t) = c_0 \vec{v}(t) + c_1 \delta \vec{a}(t) + \delta \vec{v}^G \quad . \tag{3.3}$$

The numerical coefficients c_{0-2} in these equations are given in [38] (eq. 9.20 a-c), while $\vec{r}^G$ and $\vec{v}^G$ are correlated Gaussian random numbers (see A.3Generation of Gaussian Random Numberssubsection.A.3 with zero mean value, which plays the role of thermal noise). The variances of these distributions are both temperature and time step-dependent: $\sigma_{r,v} \propto \sqrt{T}$. The detailed expressions for the variance and the correlations parameters can be found again in [38] eq. 9.23 a-c. The disadvantage of this method is the time consuming generation of random numbers, and the necessity to define a tip-mass, which is not really known yet. For the simulation presented here, a tip mass of m_{tip}=10^{-14}kg was used (the mass seems not so have a big influence anyway, as reported in [24]. Besides m_{tip}, also a damping rate $\Gamma = \frac{\gamma}{m_{tip}}$ (γ is the damping) goes into the Langevin equation. In contrast to the energy minimization method where the system is always infinite strongly damped, the damping can here be adjusted by variation of γ. Usually, the damping is expressed in terms of the critical damping $\gamma_c = 2\sqrt{\frac{k}{m_{tip}}}$. In our simulations, we chose $\gamma = 10 \times \gamma_c$.

3.3 Results

3.3.1 Energy Minimization 1D

The one dimensional model is a good tool to study the basic behavior of stick-slip motion (and to see if the algorithm works). Also to study the dynamic extension (actuation) model described by eq. (2.11Dynamic Extension of the Tomlinson Modelequation.2.11)

can be done quite easily in one dimension. Figure 3.1(a) Stick-slip curve without actuation has a much higher residual friction force than if one modulates E_0 (b). (c) Detail plot of the slip-part, indicated as the gray region in image (a). (d) The raw curve coming out of the simulation compared to a averaged curve, which corresponds to the experimental point of view. Actuation parameters: α=0.9, f=300 Hz.figure.caption.17 shows a series of such results. The model parameters were set to be E_0=0.4 eV, k=2 N/m, v=5 nm/s and a=5 $\mathring{A}$ (all the curves are "forward-scans"). Curves (a) and (b) arise from the same parameters, except that in curve (b), the actuation-parameter α has set to be 0.9 and the corresponding frequency f=300 Hz. It is important to understand that the actuation frequency is not as high as in the experiment. In fact, the actuation only acts as a tool to overcome the energy barrier ΔE between two minima of the total energy and thus the frequency can be chosen to be much smaller in the simulation (and thus saving computation time). The average friction force drops in this example from 0.45 nN (a) to 0.0011 nN (b). This behavior ("dynamic superlubricity") can be understood quite intuitively (for T=0): Since the total energy oscillates, also the energy barrier ΔE oscillates with the same frequency and since the slip occurs when $\Delta E \leq$0, this happens much sooner than in the static case. A magnification of the "slip"-part of (b) is shown in (c). Since we have two different frequencies (washboard-frequency and actuation-frequency), there is also always a phase-effect, meaning that the point where the slip occurs is not always at the same position. It has been shown [24] that over 100 slips have to be simulated in order to get reproducible average friction forces (phase effects averages out). The curve which results from the simulation are not exactly what we see if we actuate the tip in the experiment. Typically, the experimental curves are an average of the "raw" curves. Because of the high oscillation-frequency, the single oscillation can only be seen when measuring with very high time resolution (bandwidth). The friction force averaged over one oscillation period is shown in (d).

3.3.2 Energy Minimization 2D

The practical usage of a two dimensional energy minimization algorithm is much more difficult. Since the tip can now move in all directions on a plane, it is more difficult to track the energy minimum accurately on the energy surface. Therefore, numerical artifacts may occur in the friction maps. A further point to consider is the construction of a two dimensional tip-sample potential. A compact form of such a periodic potential can be approximated by the first two terms of a Fourier series of a general cubic potential ([39]):

$$V(x,y) = -\frac{E_0}{2}\left(v_1[cos(\frac{2\pi}{a}x) + cos(\frac{2\pi}{a}y)] + v_2 cos(\frac{2\pi}{a}x) \times cos(\frac{2\pi}{a}y)\right) \quad . \tag{3.4}$$

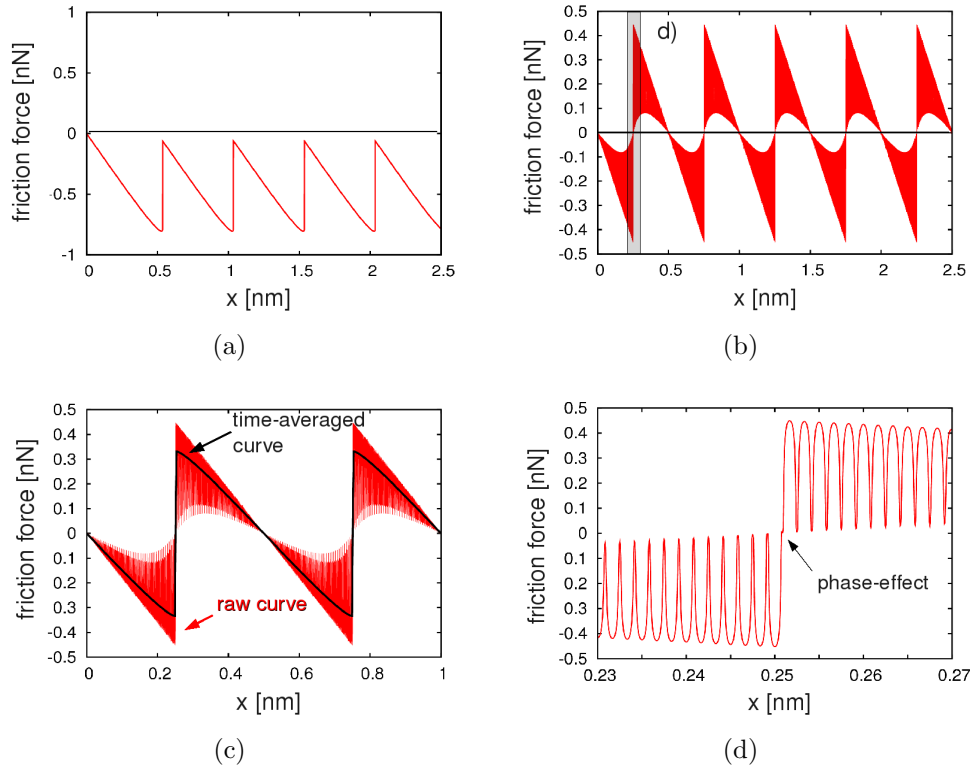

Figure 3.1: *(a) Stick-slip curve without actuation has a much higher residual friction force than if one modulates E_0 (b). (c) Detail plot of the slip-part, indicated as the gray region in image (a). (d) The raw curve coming out of the simulation compared to a averaged curve, which corresponds to the experimental point of view. Actuation parameters: α=0.9, f=300 Hz.*

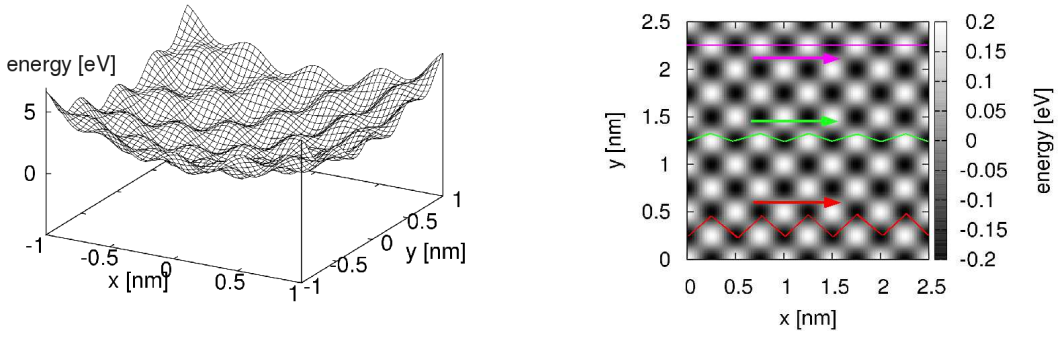

(a) (b)

Figure 3.2: *(a) Total energy of spring and surface potential in two dimensions. (b) Potential map (eq.* (3.4Energy Minimization 2Dequation.3.4) *(with v_1=0, v_2=1) and a sketch of three different path of tip movement for different ratios of k_y/k_x (red: $k_y/k_x < 1$, green: $k_y/k_x \approx 1$, magenta: $k_y/k_x \gg 1$)*

The prefactors $v_{1,2}$ are model parameters that strongly influences the shape of the potential energy surface. The total energy then becomes:

$$E(x,y) = \frac{1}{2}k_x(x - x_{sup})^2 + \frac{1}{2}k_y(y - y_{sup})^2 + V(x,y) \tag{3.5}$$

The shape of this energy is shown in fig. 3.2(a) Total energy of spring and surface potential in two dimensions. (b) Potential map (eq. (3.4Energy Minimization 2Dequation.3.4) (with v_1=0, v_2=1) and a sketch of three different path of tip movement for different ratios of k_y/k_x (red: $k_y/k_x < 1$, green: $k_y/k_x \approx 1$, magenta: $k_y/k_x \gg 1$)figure.caption.18. A point that must be considered is the fact that we now have to treat two different spring constants $k_{x,y}$ (or a "stiffness matrix" respectively), representing the total experimental stiffness of the system in the corresponding direction. The cantilever is presumably softer in the direction perpendicular to the beam direction (thus in x-direction, torison) than in the other direction (y-direction). The deformation in y-direction, the so-called "buckling", also depends on the angle ϵ between cantilever and surface. Until now, the spring constant k_y is not exactly known. But as shown in section 5.3Lateral Contact Stiffnesssubsection.5.3, the main contribution to the contact stiffness comes from tip and sample (which should be isotropic). Thus, k_y should be chosen in the same order of magnitude than k_x, or a little bit higher (e.g. by a factor of 1.1-1.4).

The first thing that now can be observed by going into two dimension is the fact that the cantilever now describes a zig-zag trajectory, always trying to avoid the maxima of the lattice energy. In figure 3.2(a) Total energy of spring and surface potential in two dimensions. (b) Potential map (eq. (3.4Energy Minimization 2Dequation.3.4) (with v_1=0, v_2=1) and a sketch of three different path of tip movement for different ratios of k_y/k_x (red: $k_y/k_x < 1$, green: $k_y/k_x \approx 1$, magenta: $k_y/k_x \gg 1$)figure.caption.18

(b), the tip path for three different ratios of k_y/k_x is shown (high: magenta, intermediate: green, low: red). The underlying gray-scale plot shows the potential for v_1=0 and v_2=1, which produced results that look best compared to the experimental ones (however, most "realistic" choice of these parameters are may be different). In fig. 3.3Friction maps (forward) of a cubic lattice with a=5 $\mathring{A}$ and E_0=1 eV. The left column shows the simulation results without actuation, while the right column is the result with actuation (α=0.9, f=500 Hz). The rows represent three different values of k_x and k_y: (a)+(b) k_x=2 N/m, k_y=0.7 N/m (c)+(d) k_x=2.0 N/m, k_y=2.5 N/m (e)+(f) k_x=2.0 N/m, k_y=5 N/mfigure.caption.19, four friction maps are shown, resulting from the simulation. The first column are images without actuation, the second column with actuation (α=0.9). It can be seen that (beside average friction reduction) the images with actuation show better the symmetry of the potential (especially for $k_y > k_x$). For the case when $k_y \approx k_x$, the difference is rather small. For the (unrealistic) case of $k_y < k_x$, the friction map consists of vertical stripes rather than the typical diamond-like shaped pattern.

Of course, all these maps are free of "noise" (since T=0 K). As shown in the next section, the temperature also acts like an actuation (100 K $\approx$ 0.1 "α"). Therefore the experimental friction are always weak "actuated" and of course more noisy (see 3.3.3Langevin Equation 1Dsubsubsection.3.3.3). The second problem is to find adequate values for the potential parameters v_1 and v_2, since they may also depend on the static load and the ionic kind of the crystal (and tip atoms!). A more numerical issue is the visualization of the data. Because the oscillation frequency is higher than the resolution of the picture (or print), the image is somehow averaged automatically.

3.3.3 Langevin Equation 1D

Using Ermak's algorithm to solve the Langevin-equation gives the possibility to study the influence of a finite temperature T. In contrast to the one dimensional figures obtained by energy-minimization, the stick-slip-curves resulting from this technique look much noisier due to thermal effects (of course, there are other sources of noise in a experiment). In fig. 3.4(a) One dimensional stick-slip curve as a result of Ermak's algorithm. Due to thermal effects, jumps do not occur at a constant $F_{L,max}$. (b) Numerical determination of a suitable time-step: Temperature is plotted against the time-step, while the color-scale indicates the averaged friction force. If the time-step is to high (>0.17 μs), the algorithm breaks down.figure.caption.20 (a), one example curve is shown. It can clearly be seen that the slips do not occur all at the same maximal lateral force $F_{L,max}$. This can be understood by the influence of thermal effects (which are stochastic). The energy barrier which separates the stick from the slip-process is now not only a function of the support position, but has also a random component. This results in slips that occur relatively late and slips that occur much earlier than in the case T=0 K (in average, they slip earlier!). It is even possible that the tip jumps back again after a slip, or that multiple slips occur. In general, the average friction force $\bar{F}_L$ is reduced with higher

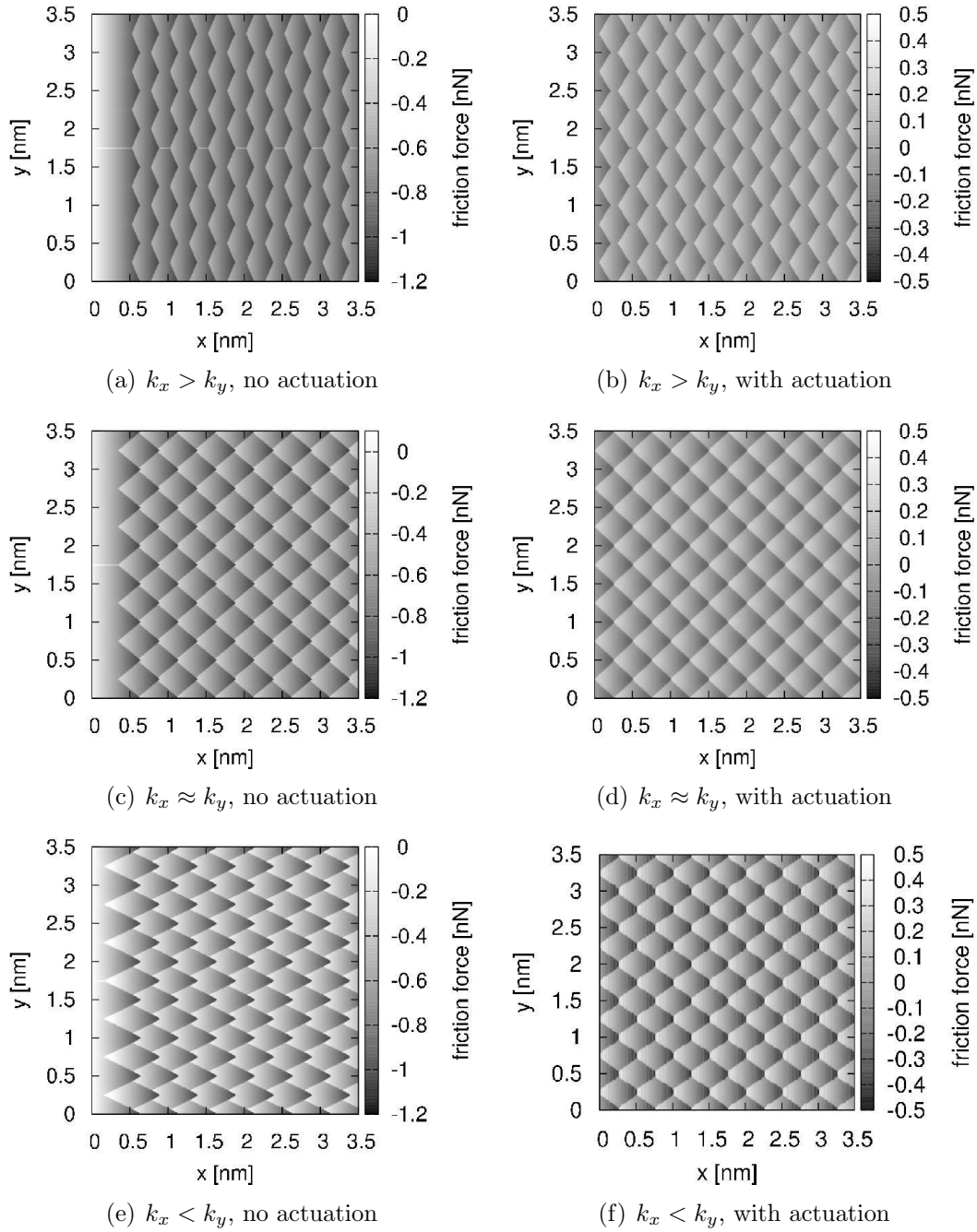

(a) $k_x > k_y$, no actuation

(b) $k_x > k_y$, with actuation

(c) $k_x \approx k_y$, no actuation

(d) $k_x \approx k_y$, with actuation

(e) $k_x < k_y$, no actuation

(f) $k_x < k_y$, with actuation

Figure 3.3: *Friction maps (forward) of a cubic lattice with a=5 Å and E_0=1 eV. The left column shows the simulation results without actuation, while the right column is the result with actuation (α=0.9, f=500 Hz). The rows represent three different values of k_x and k_y: (a)+(b) k_x=2 N/m, k_y=0.7 N/m (c)+(d) k_x=2.0 N/m, k_y=2.5 N/m (e)+(f) k_x=2.0 N/m, k_y=5 N/m*

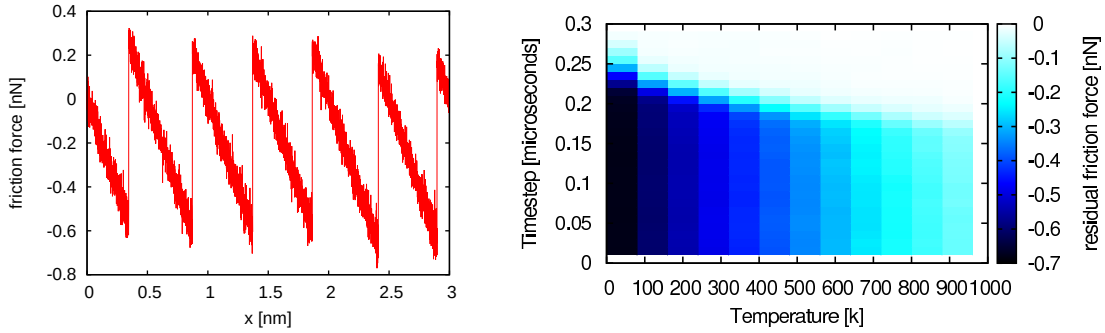

(a) (b)

Figure 3.4: *(a) One dimensional stick-slip curve as a result of Ermak's algorithm. Due to thermal effects, jumps do not occur at a constant $F_{L,max}$. (b) Numerical determination of a suitable time-step: Temperature is plotted against the time-step, while the color-scale indicates the averaged friction force. If the time-step is to high (>0.17 μs), the algorithm breaks down.*

temperatures, as described by eq. (3.6Langevin Equation 1Dequation.3.6).

Since the computation of this algorithm takes quite some time, one should think about choosing an appropriate time-step δt. For this purpose, the code has been run with different temperatures and time-steps (and a constant actuation parameter α=0.5). The result is shown in fig. 3.4(a) One dimensional stick-slip curve as a result of Ermak's algorithm. Due to thermal effects, jumps do not occur at a constant $F_{L,max}$. (b) Numerical determination of a suitable time-step: Temperature is plotted against the time-step, while the color-scale indicates the averaged friction force. If the time-step is to high (>0.17 μs), the algorithm breaks down.figure.caption.20 (b). Over a certain time-step of about 0.17 μs (depends on the temperature) $\bar{F}_L$ breaks down, while for a time-step below this threshold, the simulation shows the expected decrease of $\bar{F}_L$ with T. But further decreasing of δt did not show any improvement of accuracy. As a result, δt was chosen to be 0.10 μs.

This algorithm can now be used to study the interplay of the omnipresent thermal noise and the artificial external actuation of the cantilever (so-called "thermo-superlubricity". Therefore we have mainly a three dimensional parameter space: (α, T, η). In order to avoid phase-effects between the washboard frequency v/a and the actuation frequency f, $\bar{F}_L$ was averaged over 100 lattice spacings. The tip mass was chosen to be 10^{-14} kg and 10 times critical damped. The spring-constant was always 2 N/m. Results for η=5,8 and 15 are plotted in fig. 3.5(a)-(f) Results from the Ermak's algorithm, showing the interplay of the actuation parameter α and the temperature for three different values of η. The color-scale in the first column denotes the average friction force $\bar{F}_L$, while the second column shows the contour lines. Each of those three runs took around 30 hours to compute (on one CPU).figure.caption.21. The first column shows the averaged fiction force in color-coding, while the second column only shows the contour lines for $\bar{F}_L$ (lines where $\bar{F}_L$ is constant). Everything beyond the green line is below 0.1 nN, therefore

one may call this the border to the "superlubricity"-region. As expected, $F_{L,max}$ goes down with both α and T. The temperature dependence is closely related to the velocity dependence of friction, since $T \sim 1/v$. This dependence has been analyzed by [40, 41, 42]. According to these authors, the velocity and temperature dependence is given by

$$F_L \propto F_{L,0} - T^{2/3} ln^{2/3} \left[B \frac{T}{v} \right] \quad , \tag{3.6}$$

where $F_{L,0}$ is the friction for T=0 K. The non-universal constant B depends on the exact details of the setup. This behavior could be well reproduced numerically in this work (with α=0). Of course, the curve saturates when $\bar{F}_L \approx 0$ nN. Fully analytic solution coming out of the master-equation has recently been proposed by [43].

For T=0 K and small α, the residual friction reads ([44])

$$F_L = F_L(\alpha = 0) + \frac{\partial F_L}{\partial \eta} \eta (1 - \alpha) \quad . \tag{3.7}$$

Finding an analytical expression for the case of both non-zero α and T seems to by quite challenging. It should be possible (at least) to find solutions for extreme values of η(1-α), but this could not be done within this masterthesis. However, some information can be extracted from the simulations. The iso-friction lines in the (α,T)-plane has a slope $\frac{\Delta\alpha}{\Delta T}$ of about 0.11-0.25 $\frac{1}{100K}$ (η=5), 0.065-0.17 $\frac{1}{100K}$ (η=8) and 0.005-0.07 $\frac{1}{100K}$ (η=8). The first number denotes the slope of the line $\bar{F}_L$=-0.1 nN while the second number gives the slope of $\bar{F}_L$=-1 nN. Thus, for intermediate values of α and η, an actuation of α=0.1 corresponds approximately to a temperature increase of 100 K.

3.3.4 Langevin Equation 2D

The extension of the one dimensional code into two dimension is straight forward. All the parameters has to be defined in y-direction similar to the x-direction (e.g. thermal noise, velocity, acceleration....). Again, the same potential was used as described in section 3.3.2Energy Minimization 2Dsubsubsection.3.3.2. Since the results are almost similar to those in fig. 3.3Friction maps (forward) of a cubic lattice with a=5 $\mathring{A}$ and E_0=1 eV. The left column shows the simulation results without actuation, while the right column is the result with actuation (α=0.9, f=500 Hz). The rows represent three different values of k_x and k_y: (a)+(b) k_x=2 N/m, k_y=0.7 N/m (c)+(d) k_x=2.0 N/m, k_y=2.5 N/m (e)+(f) k_x=2.0 N/m, k_y=5 N/mfigure.caption.19, we do not have to go into details at this point. The main differences are the reduction of the mean friction as discussed in the last section, and the noise that apperars in the friction map. The influence of the temperature is again shown in fig. 3.6(a)-(c) Comparison between friction maps at temperatures of 0 K, 300 K and 600 K. The increase of noise is clearly visible. The

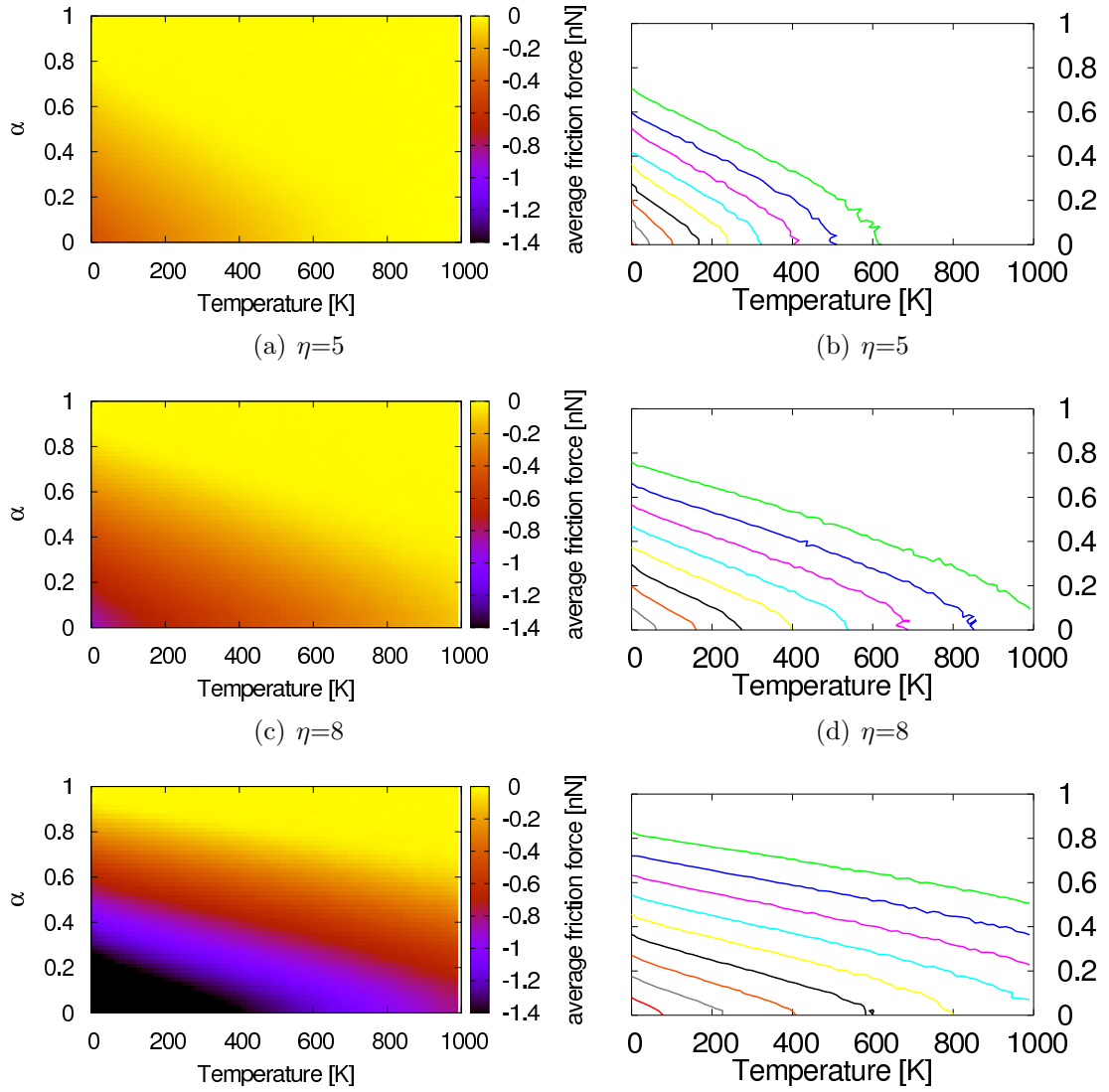

(a) η=5 (b) η=5

(c) η=8 (d) η=8

(e) η=15 (f) η=15

Figure 3.5: *(a)-(f) Results from the Ermak's algorithm, showing the interplay of the actuation parameter α and the temperature for three different values of η. The color-scale in the first column denotes the average friction force $\bar{F}_L$, while the second column shows the contour lines. Each of those three runs took around 30 hours to compute (on one CPU).*

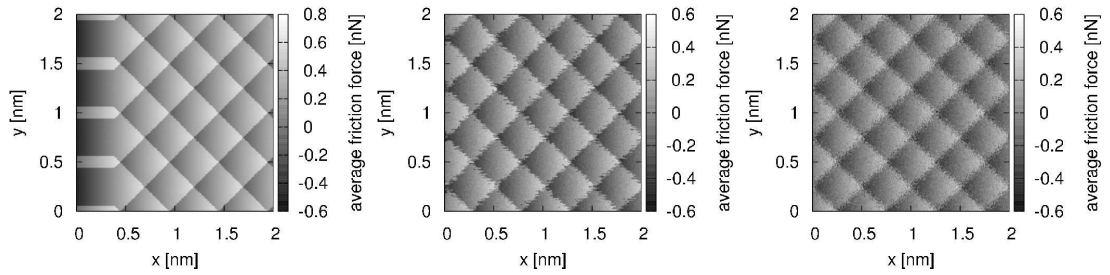

(a) T=0 K (b) T=300 K (c) T=600 K

Figure 3.6: *(a)-(c) Comparison between friction maps at temperatures of 0 K, 300 K and 600 K. The increase of noise is clearly visible. The strange artifacts in the sticking-part are typical for zero-temperature simulations (also reported by [45]. Parameters: η=4, k_x=2 N/m, k_y=2.5 N/m, v=10 nm/s, m_{tip}=10^{-13} kg*

strange artifacts in the sticking-part are typical for zero-temperature simulations (also reported by [45]. Parameters: η=4, k_x=2 N/m, k_y=2.5 N/m, v=10 nm/s, m_{tip}=10^{-13} kgfigure.caption.22, where the same simulation has been run with different temperatures. However, the noise produced in the simulation is much more isotropic distributed compared to real experiments, where mainly the scanning-direction (y-direction) is noisy. This noise may has a different origin than thermal vibrations.

A direct comparison between the two simulation methods and the experiment is shown in fig. 3.7Qualitative comparison of the friction pattern between those produced by simulations and an experimental friction map of KBr (taken from [24]). As a consequence of the thermal noise capabilities of the Ermak algorithm, this friction map looks more realistic than the one from the energy-minimization code.figure.caption.23, where the theoretical friction maps (k_x=2 N/m, k_y=2.5 N/m, E_0=0.2 eV) reproduce the experimental friction map (KBr, low load) quite well.

3.4 Outlook

There are many ways to improve the discussed models. For example by introducing two springs (in each dimension), or by considering multiple asperities (tips). In order to investigate the friction on graphite or mica, one could (and this has been done by [45]) calculate the effect of a flake attached to the tip (commensurabtility). The analytical way to analyze friction is to solve the so-called master-equation or rate-equation, but this becomes very complex when calculating with actuation and temperature. In future, it would be important to simulate friction in terms of atomistic simulations. Recent progress in this field ([46]) show the capabilities of these (computer-time consuming) technique. The main advantage is the fact that no empirical tip-sample potential and contact-stiffness is needed as a input parameter, since the relevant forces result directly from the interatomic potential (e.g. it arises directly from tip-sample interactions). Even within this one spring model, there are several things that should be improved. The most important

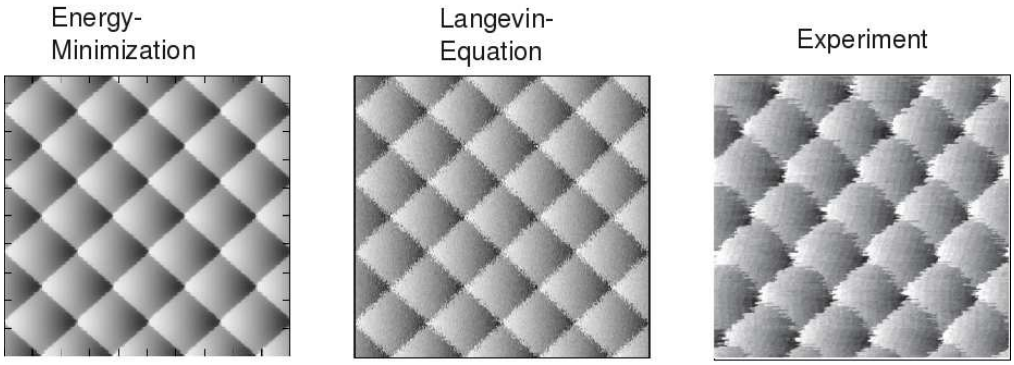

Figure 3.7: *Qualitative comparison of the friction pattern between those produced by simulations and an experimental friction map of KBr (taken from [24]). As a consequence of the thermal noise capabilities of the Ermak algorithm, this friction map looks more realistic than the one from the energy-minimization code.*

thing seems to be the (theoretical or experimental) evaluation of k_y. In order to compare simulation and experiments, also the parameter η should be defined in two dimension, which is not straight forward.

4 Experimental Setup

4.1 UHV System

The measurements presented in this work were done with a home-built AFM operated in ultrahigh vacuum (UHV) environment at room temperature. The system shown in fig. 4.1Overview of the Nanolino UHV system: On the left side the A-chamber can be seen (a) with the AFM/STM (b), the LEED/AES system (c) and the XPS (d). The P-chamber (e) is located on the right. Also visible on the picture are the sputter gun (f), the three cell evaporator (g), the atom source gun (h) and the quartz micro-balance (i). Picture taken from [47].figure.caption.24 is basically divided into three parts separated by valves: Quick-lock chamber, preparation chamber (P-chamber) and analysis-chamber (A-chamber). In order to move things from one chamber to the other, there are several transfer-arms (manipulators).

The **quick-lock** contains a quick release fastener flange for the introduction of up to three cantilevers and/or samples. It also contains an oxygen heating stage and is connected to a small turbomolecular pump (turbo pump) which is able to evacuate down to a pressure p$< 1 \times 10^{-7}$ mbar.

In the **P-chamber**, which is connected to a larger turbo pump, the preparation of samples and cantilevers (see 4.6Sample and Cantilever Preparationsubsection.4.6) takes place. Additionally, this chamber is evacuated with an ion-getter pump and a titan-sublimation pump. There are several tools available for in-situ preparation. The cleavage-knife allows to create almost atomic flat ionic crystal surfaces. The three-cell molecular evaporator allows to deposit ultrathin films of salt and molecules on the sample. A quarz-microbalance device is used to calibrate the deposition rate. In order to heat up the samples, the manipulator has a electron beam heater as well as a resistive heater. For surface preparation, the system is equipped with a sputter gun used for the preparation of metallic samples by Ar-sputtering and annealing cycles.

In the **A-chamber**, the analysis of the prepared samples is carried out with the combined AFM/STM. In the carousel, 8 samples/cantilevers can be stored and exchanged quickly. Like the P-chamber, the A-chamber is evacuated using an ion-getter pump and a titan-sublimation pump. For further sample analysis, there are several devices installed: LEED (Low Energy Electron Diffraction), AES (Auger Electron Spectroscopy), and XPS (X-ray Photo-electron Spectroscopy). In order to move objects in the chamber (e.g. from carousel into the AFM), a so-called wobbelstick allows more or less accurate manipulations.

In both the P- and A-chamber, the pressure is normally (if not heating, sputtering or cleaving) $< 1 \times 10^{-10}$ mbar.

4.2 Microscope

The AFM is built on a platform suspended by four springs and damped by an eddy current damping system in order to decouple it from external mechanical vibrations.

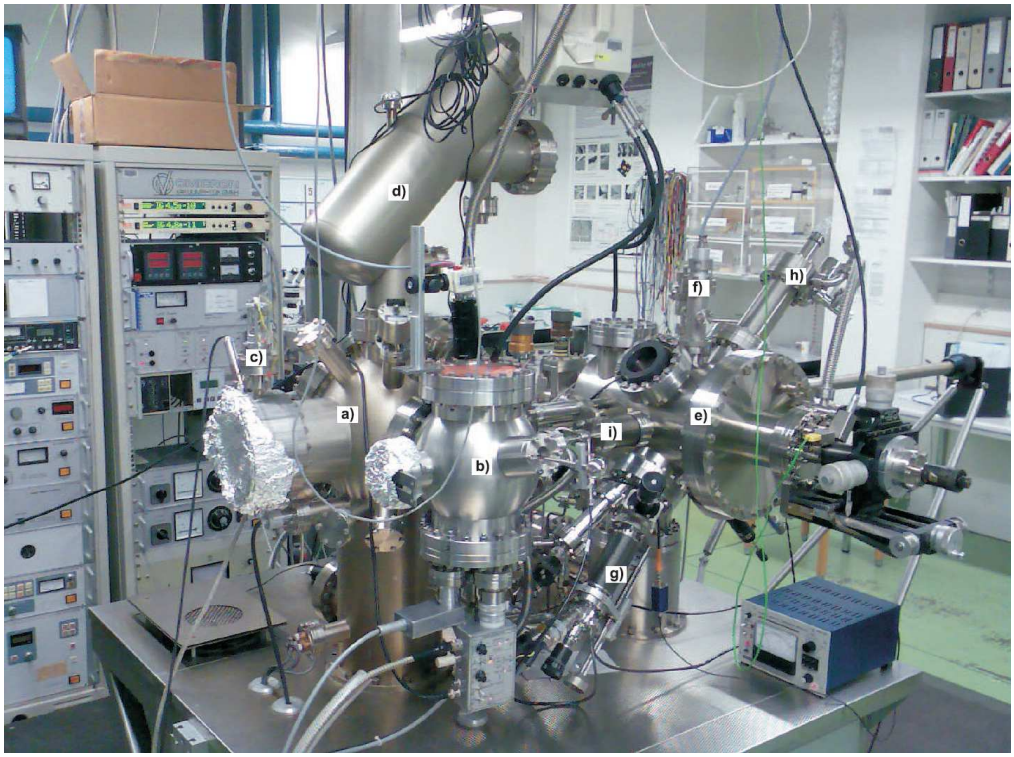

Figure 4.1: *Overview of the Nanolino UHV system: On the left side the A-chamber can be seen (a) with the AFM/STM (b), the LEED/AES system (c) and the XPS (d). The P-chamber (e) is located on the right. Also visible on the picture are the sputter gun (f), the three cell evaporator (g), the atom source gun (h) and the quartz micro-balance (i). Picture taken from [47].*

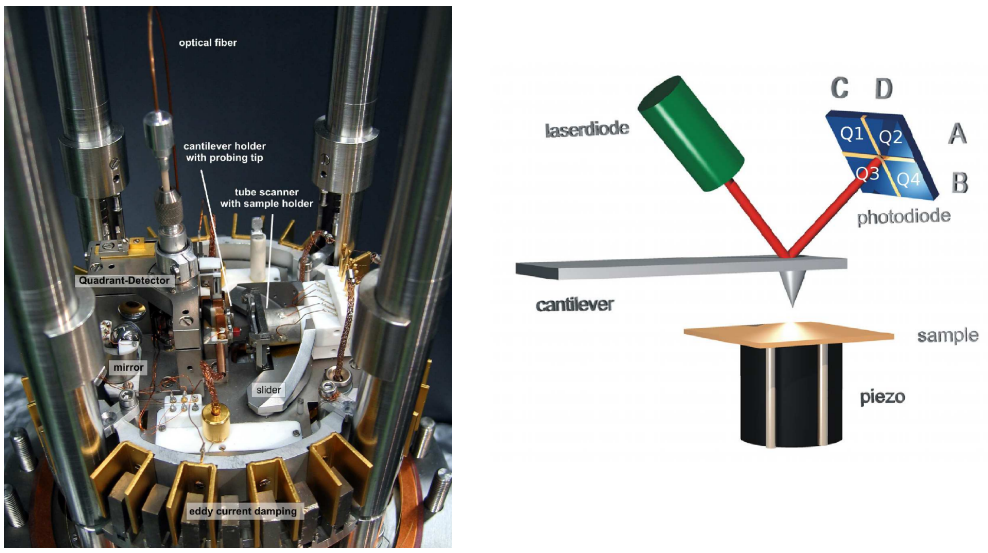

(a) (b)

Figure 4.2: *(a) Picture of the combined home-built AFM/STM. In order to improve visibility, this photo was taken when the AFM was outside the UHV-chamber. (b) Schematic view of the microscope with beam-deflection method, taken from [24].*

Its construction is based on a prototype build in 1993 [48]. The deflection of the cantilever is detected by the optical beam deflection method, which allows us to measure the normal and lateral bending of the lever simultaneously. A superluminescent diode placed outside the microscopy delivers a light beam through a glass fibre, which is then focused by a lens and guided over a mirror (mirror A) to the back of the cantilever and from there over another mirror (mirror B) to the position sensitive 4-quadrant photodiode. Piezo-motors allow to move both mirrors in any direction. The signal from the photodiode is then pre-amplified directly in UHV to guarantee a low level of additional noise. The sampling rate of the preamplifier is 3 MHz, which allows to measure with a very high time-resolution. The sample-holder sits in front of a tube piezo, which performs the scan movement while the tip remains fixed. Both sample and piezo tube are attached to a platform (walker) which can be moved by three piezos for a coarse approach. The cantilever-holder is glued on a shaking piezo in order to excite the cantilever both in nc-AFM and contact-AFM. All the piezo motors can be driven by a function-generator delivering a sawtooth-like signal at a certain frequency, which has to be chosen accurately to move the motors precisely.

There are mainly three different signals (voltages) coming from the four quadrants Q1-Q4 (see fig. (b)) of the photodiode, being produced due to the photoelectric effect. As a convention, we use A=Q1+Q2, B=Q3+Q4, C=Q1+Q3 and D=Q2+Q4. The signal A-B ("top-bottom") is called vertical deflection and corresponds to the normal force, while the signal C-D ("left-right") is called horizontal deflection and corresponds to the lateral force. The sum signal $\sum Q_i$ =A+B=C+D

is used to adjust the laser, since a maximal sum signal delivers a maximal sensitivity.

4.3 Electronics

The main parts of the electronics (besides pump controllers etc.) are the following: After being preamplified, the signals Q1-Q4 from the photodiode is again amplified and split up into A-B and C-D outside the microscope with a quadrant-detector (amplification-gain=4). At this point, the vertical deflection signal may passes a low-pass filter in order to get rid of the cantilever oscillation while approaching. Then the signal is fed into a analog-digital (AD) converter, which allows to obtain the data with the commercial AFM software running on a common desktop computer. The feedback signal produced with the software passes through the home-built digital-analog (DA) converter together with die x-y signal, going into the high-voltage (HV) amplifier. Afterwards, the signal for the x-,y- and z-piezo is again fed into the microscope. A phase-locked loop (PLL) is used to detect the eigenfrequency of the cantilever (from A-B signal) to feed again the adjusted oscillation signal to the shaking piezo of the AFM. The PLL is able to track the frequency shift Δf of the cantilever very accurately (mHz) and contains a very stable oscillator. Additionally, an oscilloscope is used to check signal quality and to obtain a quick overview of the different signals involved in this circuit. The experiments presented in this work were made using a PLL, AD/DA converter and SPM software from Nanonis [49].

4.4 Cantilever Description and Properties

Rectangular commercial available silicon cantilevers from Nanoworld (as shown in fig. 4.3Scanning electron pictures of a "CONTR" cantilever. Overview image showing the chip with cantilever and upward facing probing tip. The length of the cantilever is 476 μm. The third detail image shows of a new tip with a curvature radius of less then 8 nm. This tip has a height of 12.5 μm, what is in agreement with the range given in tab. 1Properties of the microfabricated "CONTR" cantilevers from the manufacturer Nanoworld. The 3^{rd} column shows the experimental values (SEM measurement) of the cantilever used for the NaCl on Cu(111) experiments. For the quantities that are not accessible experimentally, the mean value of the 2^{nd} column was used.table.caption.26figure.caption.27) were used for contact-AFM measurements. These micofabricated levers are highly n-doped to allow both AFM and STM measurements. In contrast to cantilevers used for nc-AFM, contact cantilevers are much softer (k $<$ 1 N/m compared to several 10 N/m), since they are longer and thinner. A low spring constant is favorable for contact-AFM, since for a given noise-level, smaller forces are detectable. Triangular cantilevers are also widely used, but because of their more complicated geometry, analytical stiffness calibration is more difficult. A table of the cantilever details delivered by the manufacturer [49] is given in table **??**Calibrationtable.caption.30.

technical data	range		measured	
thickness t	1.5-2.5	μm	1.67	μm
width w	45-55	μm	50	μm
length L_1	445-455	μm	451	μm
length L'	no info		24.8	μm
tip height h	10-15	μm	12.5	μm
force constant k_N	0.07-0.4	N/m	0.107	N/m
resonance frequency f_0	9-17	kHz	11.325	kHz

Table 1: *Properties of the microfabricated "CONTR" cantilevers from the manufacturer Nanoworld. The 3rd column shows the experimental values (SEM measurement) of the cantilever used for the NaCl on Cu(111) experiments. For the quantities that are not accessible experimentally, the mean value of the 2nd column was used.*

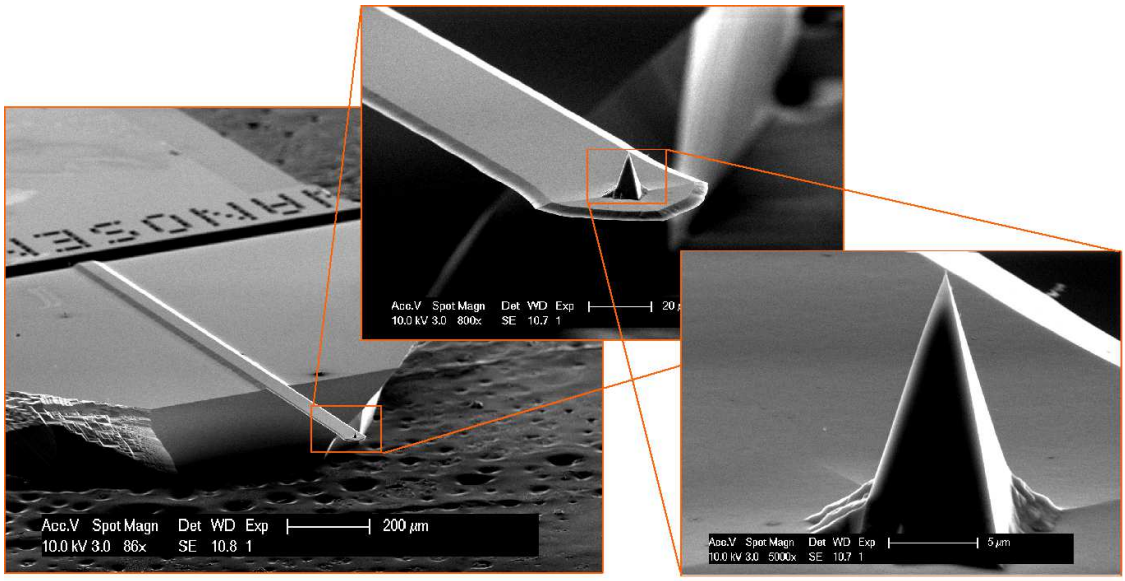

Figure 4.3: *Scanning electron pictures of a "CONTR" cantilever. Overview image showing the chip with cantilever and upward facing probing tip. The length of the cantilever is 476 μm. The third detail image shows of a new tip with a curvature radius of less then 8 nm. This tip has a height of 12.5 μm, what is in agreement with the range given in tab. 1Properties of the microfabricated "CONTR" cantilevers from the manufacturer Nanoworld. The 3rd column shows the experimental values (SEM measurement) of the cantilever used for the NaCl on Cu(111) experiments. For the quantities that are not accessible experimentally, the mean value of the 2nd column was used.table.caption.26*

There exist different methods to determine the stiffness of cantilevers. For example, one can add an additional mass on the tip and observe its change in resonance frequency (Cleveland-method) [50]. Its also possible to make use of a surrounding fluid (e.g. air) which damps the motion (Sader-method [51]). However, for rectangular beams in UHV, analytical expressions both for the normal stiffness k_N and the torsional stiffness k_T can be found [52] and proofed to be quite good (although material properties must be known):

$$k_N = \frac{Ewt^3}{4L_1^3} \qquad k_T = \frac{Gwt^3}{3h^2L_1} \quad . \tag{4.1}$$

Here, E is the Young's modulus, G the shear modulus, L_1 the length from chip to the center of the tip, w the width, t the thickness and h the tip-height. In order to eliminate the big uncertainty of the thickness delivered by the manufacturer (2μm $\pm 0.5\mu$m) , it is common to calculate the thickness out of the eigenfrequency (first mode) f_0 of the free cantilever [52], which can be obtained either by recording the thermal power-spectrum or by sweeping the actuation frequency:

$$t = \frac{2\sqrt{12}\pi}{k_{1,free}^2}\sqrt{\frac{\rho}{E}}f_0 L^2 \quad . \tag{4.2}$$

The wavenumber $k_{1,free}$ for the first oscillation mode is 1.8751 and $L = L_1 + L'$ denotes the total lenght of the cantilever. For the material constants following values were used: $E = 1.69 \times 10^{11} N/m$, $G = 6.8 \times 10^{10} N/m$ and $\rho = 2.323 \times 10^3 kg/m^3$.

Recording the power spectral density (PSD) of the cantilevers thermal noise (see fig. 4.4Typical thermal spectrum of a cantilever. The red line is the vertical deflection, while the green line shows the horizontal deflection (torsion). All these peaks can be seen in both channels, since a crosstalk between them can not be completely eliminated.figure.caption.28) reveals the first few vibration modes simultaneously. The PSD for the n'th eigenmode is given by [53]:

$$S_n(\omega) = \frac{2k_B T\omega_n^3}{Qk_{n,N}\left[\left(\omega^2 - \omega_n^2\right)^2 + \frac{\omega_n^2\omega^2}{Q^2}\right]} \tag{4.3}$$

Here, Q is the quality factor, T the temperature, $k_{n,N}$ the normal spring-constant and ω_n the frequency of the n'th eigenmode and k_B the Boltzmann constant. This relation allows to determine the spring constant of the cantilever in an alternative way than eq. (4.1Cantilever Description and Propertiesequation.4.1). The quality factor reaches values $> 400'000$ in UHV, while oscillating in air $Q \approx 100$. Methods to determine the Q-factor are described in the appendix A.1Q-Factor Determinationsubsection.A.1.

4.5 Calibration

The next step include the calibration of the (vertical) sensitivity s_Z of the system, which depends mainly on the position of the laser spot on the cantilever and the

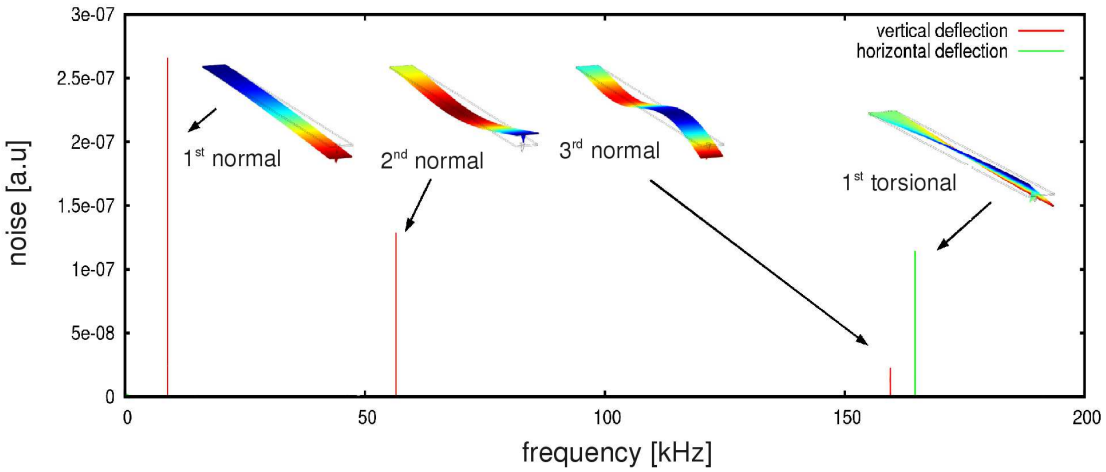

Figure 4.4: *Typical thermal spectrum of a cantilever. The red line is the vertical deflection, while the green line shows the horizontal deflection (torsion). All these peaks can be seen in both channels, since a crosstalk between them can not be completely eliminated.*

optical properties of the cantilever surface (thus the sum signal). A maximal sensitivity can be obtained (for a given photodiode) if using a cantilever with a reflex coating (raises s_z by a factor of 2) and a laser spot positioned as far at the front end as possible. To determine the sensitivity quantitatively, a force-distance-curve is used, where the slope of the linear part gives s_Z in m/V (V is the voltage of the vertical deflection U_{A-B}), since the Z-piezo of the scanner is already calibrated independently. Using eq. (4.1Cantilever Description and Propertiesequation.4.1) and s_Z allows to transform measured quantities (these are namely vertical deflection U_{A-B} and horizontal deflection U_{C-D}) into forces:

$$F_N = k_N s_Z U_{A-B} \quad . \tag{4.4}$$

The calibration of the lateral force is not straight forward, since only the sensitivity in vertical direction is known. There exists a bunch of different calibration methods to determine the lateral sensitivity experimentally. Most of them include a *colloidal test probe* which is then scanned over a sample of knwon geometry [54]. However, by using rectangular cantilevers, geometric assumptions allows to calculate the lateral force analytically [55]:

$$F_L = \frac{3}{2} k_T \frac{h}{l} \frac{s_Z}{m} U_{C-D} \quad , \tag{4.5}$$

where h and l are the tip height and the length of the cantilever, respectively. The factor m represents the shape of the laser spot on the photodiode and is only ewual to 1 if the spot is circular. Since measurement of m also includes special probes, $m = 1$ has been chosen in this work [56, 24]. A further problem for quantitative data analysis is the crosstalk between the two channels, since the cantilever, the sample and the photodiode are not perfectly aligned. For a free cantilever, the normal vibration is clearly visible in the horizontal signal, while

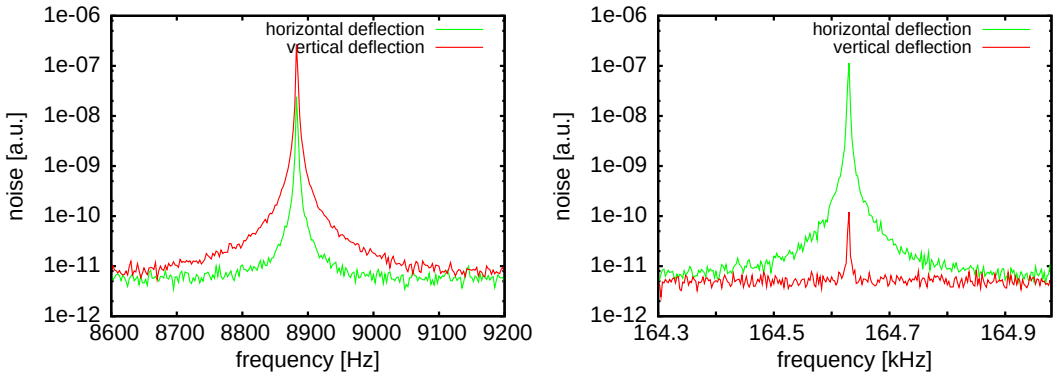

Figure 4.5: *A logarithmic plot of the first normal vibration mode (a) and first torsional mode (b) is shown here. Clearly visible is the crosstalk between the two channels U_{A-B} and U_{C-D}*

the torsional signal is not much pronounced in the vertical signal as fig. 4.5A logarithmic plot of the first normal vibration mode (a) and first torsional mode (b) is shown here. Clearly visible is the crosstalk between the two channels U_{A-B} and U_{C-D}figure.caption.29 shows. However, there is allways a crosstalk in both directions. When doing friction experiments, the topography often has a imprint of the frictional contrast, especially at step edges. A dynamical solution for this problem was proposed by Matei et. al [57].

For the presented work, the following calibration was used:

normal f_0	11325	Hz
normal stiffness	0.107	N/m
lateral stiffness	68.7	N/m
vertical sensitivity	1.46×10^7	V/m
vertical calibration	73.49	nN/V
lateral calibration	202	nN/V

4.6 Sample and Cantilever Preparation

For our experiments, we used a copper single crystal cut along the (111) direction and polished with a high accuracy (Mateck GmbH- Jülich, Germany). In order to clean the substrate, several Ar^+ bombardment (sputtering) and subsequent annealing cycles (520 ^{o}C) were applied. Having now an almost clean and flat surface, the evaporation of NaCl can take place. In order to deposit a certain amount of material with the three-cell evaporator, the evaporation rate must be calibrated using a quarz-microbalance. This oscillating quarz is exposed to the evaporation cone, whereby its oscillation frequency changes due to mass deposition. Doing this under different thermal conditions, the evaporation rate at a certain temperature

can be quantified. Choosing an evaporation temperature of 400 ^{o}C results in a deposition rate of 0.4 $\mathring{A}$/min. Therefore 15 minutes it should be enough to deposit an average NaCl coverage of 6 $\mathring{A}$ or $\approx$ 2 monolayer (ML), while keeping the substrate at a constant temperature of 100 ^{o}C.

Cantilever preparation consist of first gluing the chip on the cantilever-holder (titanium block) in air with an conductive two-component glue which must be baked for hardening at 150 ^{o}C for 1 hour. After transferring it into the microscope, the cantilever is heated up to 120 ^{o}C for 30 minutes to remove water and dirt. Tip sputtering, usual done for nc-AFM, was not applied for this contact-measurement.

5 Results

5.1 Thin films growth

The growth mechanism of ultra-thin alkali halide films have been studied by many research groups [58, 59, 60, 47, 61]. First of all, one observes a carpet-like growth of big NaCl Island (stretch of lattice constant) with a typical size of several hundreds of nanometers, smoothly overgrowing the substrate, while three different orientations are possible.

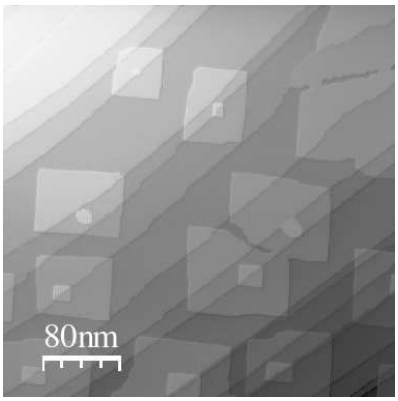

(a) Topography

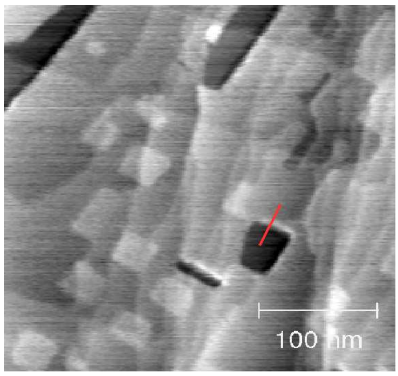

(b) Topography

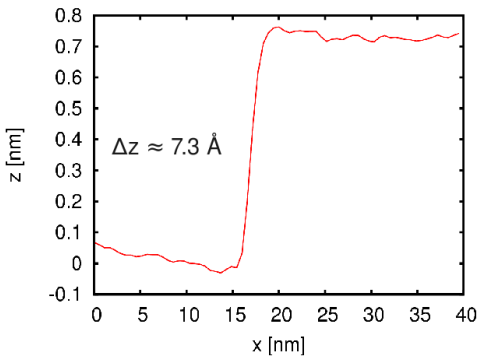

(c) Profile

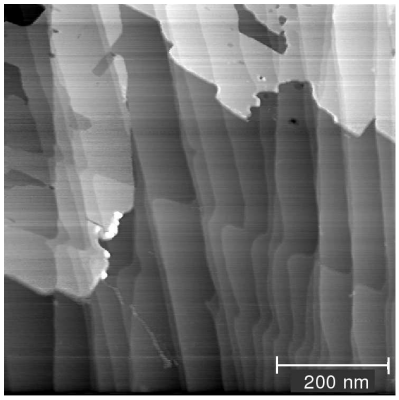

(d) Topography

Figure 5.1: *(a) Image recorded with non-contact mode showing rectangular NaCl islands on Cu(111) covered with NaCl. (b) Same scenario as in (a), but imaged in contact mode. The overall topography quality is inferior to nc-AFM. The dark spots represents the copper substrate, overgrown by a bi-layer NaCl. On the NaCl carpet, ≈ 20 x 20 nm^2 large 2nd layer island are gowning. (c) Profile over a edge shows the multi-layer nature of the first layer, with over 0.72 nm in height. (d) 700 x 700 nm^2 overview image of a region where no higher island were found in contact mode.*

A lot of discussion whether the first "layer" is a mono- or bi-layer happened in the past and could not be answered conclusively. The bulk 3D lattice constant of NaCl is a =5.65 $\mathring{A}$. However, in these measurements, the height of the first layer

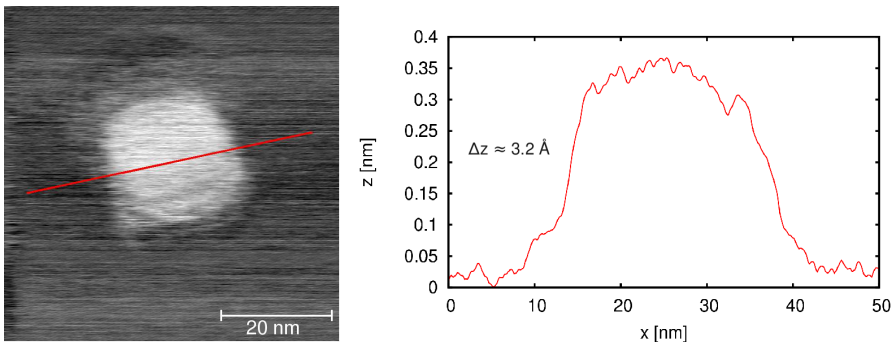

(a) Topography (b) Profile

Figure 5.2: *(a) 60 x 60 nm^2 topography image of a 2^{nd} layer island grown on the underlying NaCl bi-layer. (b) A profile taken over the hole island reveals a height of ≈ 2.6-3.4 Å and a side-length of about 30 nm*

.

varied between 0.65 nm and 1.2 nm (most frequent are step heights of ≈ 7.2 $\mathring{A}$) excludes a monolayer-layer growth (see fig. 5.1(a) Image recorded with non-contact mode showing rectangular NaCl islands on Cu(111) covered with NaCl. (b) Same scenario as in (a), but imaged in contact mode. The overall topography quality is inferior to nc-AFM. The dark spots represents the copper substrate, overgrown by a bi-layer NaCl. On the NaCl carpet, ≈ 20 x 20 nm^2 large 2^{nd} layer island are gowning. (c) Profile over a edge shows the multi-layer nature of the first layer, with over 0.72 nm in height. (d) 700 x 700 nm^2 overview image of a region where no higher island were found in contact mode.figure.caption.31). It is especially difficult to claim exact values of the first layer, since strong frictional contrast (see 5.2Frictionsubsection.5.2) between the two materials may influence the topography controller. Additionally, a different contact potential between the salt and the metal may have a strong influence in contact mode (the z-piezo calibration was done in nc-mode by measuring NaCl steps on a bulk crystal). Other measurements on NaCl as well as on KBr give rise to the conclusion, that the evaporation conditions (e.g. temperature of substrate) determine whether a mono- or bi-layer growth takes place. One has to mention that especially in contact mode, the possibility to move or to destroy the first layer is very high [61]. These two facts imply that the ionic thin film only weakly interact with the underlying substrate. If one compares images taken in nc-AFM with such taken in contact mode, it can be seen that the impact of the tip results in more round-shaped corners.

On the first bi-layer, sometimes smaller 2^{nd}-layer islands are growing, with a typical rectangular shape with a width of about 15-30 nm and a height of 2.6-3.4 $\mathring{A}$. The value measured for this islands matchs good with $a/2$=2.83 $\mathring{A}$.

This additional islands are much stronger bound than the first layer, hence less endangered to be destroyed while scanning. The growth direction seems to be the same as the underlying NaCl bi-layer. As mentioned above, scanning such weakly bound systems need special attention. In order to harm the thin films

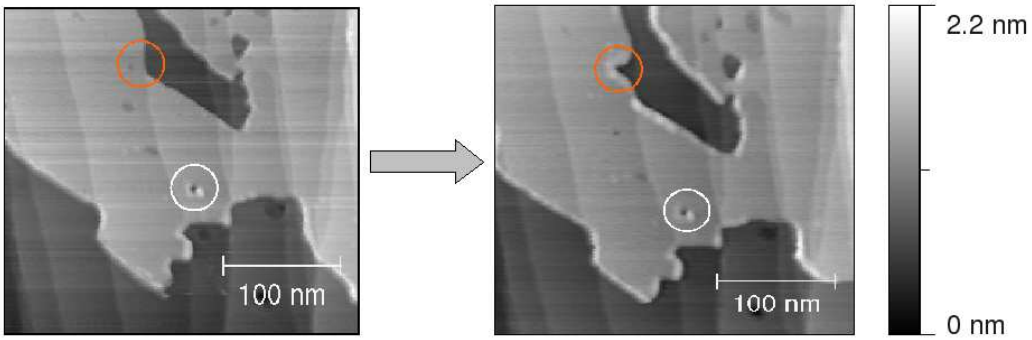

Figure 5.3: *300 x 300 nm^2 topography image showing wear at the border between Cu(111) and NaCl (orange circle). The white circles show local defects on the salt film which are also caused by scanning or by approaching.*

(especially the border between Cu(111) and NaCl) as less as possible, we made use of two different methods to reduce wear. On one hand, a very small normal static force was chosen, on the other hand, we excited the 1^{st} normal vibration mode of the cantilever in order to reduce friction and wear [62]. From now on, the term "excitation" always means mechanical excitation with a shaking piezo. It is also indispensable to let the tip equilibrate, meaning to be patient until stable tip conditions set in. We experienced especially good results by scanning first in a very small area of the same material (e.g. 10 x 10 nm^2) until tip-changes become rare, and then go subsequently to larger scales. An example what could happen is shown in fig. 5.3300 x 300 nm^2 topography image showing wear at the border between Cu(111) and NaCl (orange circle). The white circles show local defects on the salt film which are also caused by scanning or by approaching.figure.caption.33, where the same 300 nm wide region is imaged before and after scanning the border regions. Also small defects on the NaCl-layer are visible which probabely come from scanning/approaching.

5.2 Friction

5.2.1 Friction at the μm-Scale

Scanning perpendicular to the cantilever elongation allows to obtain frictional contrast, corresponding to a sideways twist if the tip. Obviously, the friction is highly enhanced at material steps, which acts as high geometrical energy barriers. The biggest contrast can therefore be seen between Cu(111) and the first NaCl bi-layer (heighest step). But also 2^{nd} layer island and steps in the substrate produce strong contrasts. Even the Cu(111) steps overgrown by the NaCl carpet are clearly visible in the horizontal deflection images (see fig. 5.4(a)+(b) Forward and backward scan of a 600 x 600 nm^2 region with low coverage. Clearly enhanced contrast at steps, even the steps in the copper crystal are visible through the NaCl carpet in the upper part of the images. The average friction on Cu(111) is negligible compared

to the corresponding values on NaCl. On all the images, Cu(111) is bright in the forward scan while NaCl is darker. Parameters: F_N=-0.7 nN, excitation=200 mV. (c)+(d) Forward and backward scan of a 700 x 700 nm^2 region with higher coverage (>2 ML). Parameters: F_N=2.3 nN, excitation=10 mV. (e)+(f) Forward and backward scan of a 700 x 700 nm^2 region. Parameters: F_N=0 nN, excitation=10 mV. figure.caption.34). As a matter of fact, the contrast in friction-images are inverted when comparing forward to backward channel. In a forward image, a lower friction signal (more negative!) correspond to a higher friction, while in backward scans, a higher frictional signal correspond to a higher friction force. When taking the absolute values $|F_L|$, then forward and backward images looks more or less identical. By exciting the cantilever at its contact resonance frequency ($\sim$ 56 kHz, see section 5.4Contact Dynamicssubsection.5.4) and therefore reducing friction, the absolute friction force values are not anymore comparable within different images, when conditions and/or excitation settings may have changed. Therefore, care must be taken when comparing the results quantitatively.

It can be seen in fig. 5.4(a)+(b) Forward and backward scan of a 600 x 600 nm^2 region with low coverage. Clearly enhanced contrast at steps, even the steps in the copper crystal are visible through the NaCl carpet in the upper part of the images. The average friction on Cu(111) is negligible compared to the corresponding values on NaCl. On all the images, Cu(111) is bright in the forward scan while NaCl is darker. Parameters: F_N=-0.7 nN, excitation=200 mV. (c)+(d) Forward and backward scan of a 700 x 700 nm^2 region with higher coverage (>2 ML). Parameters: F_N=2.3 nN, excitation=10 mV. (e)+(f) Forward and backward scan of a 700 x 700 nm^2 region. Parameters: F_N=0 nN, excitation=10 mV. figure.caption.34 (a)/(b) that especially on NaCl tip changes frequently happened. This may occur from scanning over two different materials, such that the tip apex is not always contaminated with atoms of the same species. Because of this specialty, it is very difficult to obtain good resolution at step edges. It seems that under these circumstances, the tip has not enough time to reach stable conditions. As shown in figure 5.5(a) Friction image showing Cu(111) on the left side, while on the right side, the NaCl carpet starts. Compared to the quite acceptable resolution on the copper, the NaCl region does not reveal the atomic lattice. (b) Topography image of another border region, showing the elevation at the edge, probably coming from scratching away material. figure.caption.35, the resolution on Cu(111) is fairly good, but the NaCl cannot be resolved atomically. Another interesting observation is the additional elevation at NaCl step edges, as shown in fig. 5.5(a) Friction image showing Cu(111) on the left side, while on the right side, the NaCl carpet starts. Compared to the quite acceptable resolution on the copper, the NaCl region does not reveal the atomic lattice. (b) Topography image of another border region, showing the elevation at the edge, probably coming from scratching away material. figure.caption.35 (b). They may occur because of deposition of moved material, or due to too strong z-controller settings. Nevertheless, there is also a contribution to this behavior which comes from the edge itelf (uncompensated electrostatic forces), as reported by [59, 60] using nc-AFM and STM respectively.

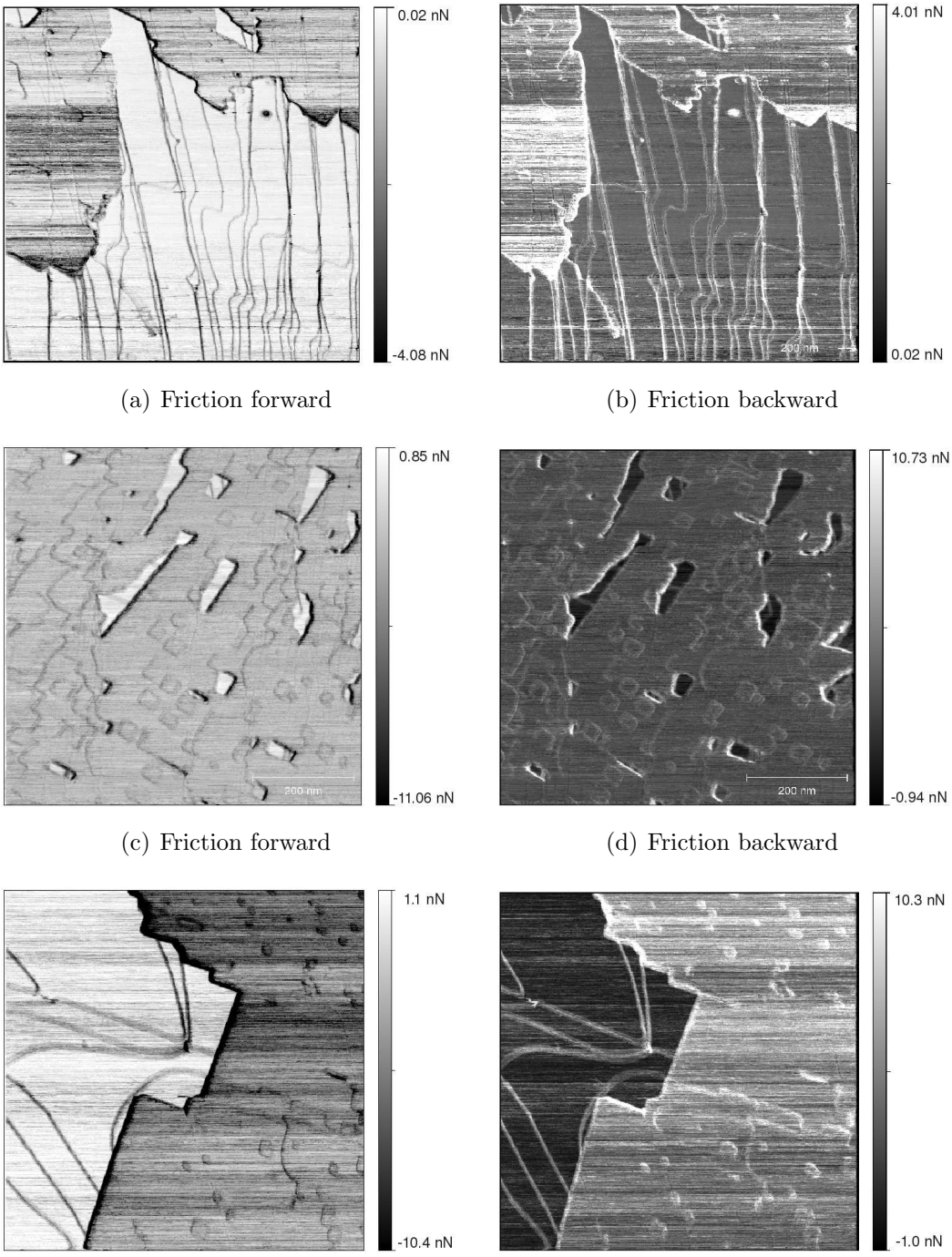

(a) Friction forward (b) Friction backward

(c) Friction forward (d) Friction backward

(e) Friction forward (f) Friction backward

Figure 5.4: *(a)+(b) Forward and backward scan of a 600 x 600 nm^2 region with low coverage. Clearly enhanced contrast at steps, even the steps in the copper crystal are visible through the NaCl carpet in the upper part of the images. The average friction on Cu(111) is negligible compared to the corresponding values on NaCl. On all the images, Cu(111) is bright in the forward scan while NaCl is darker. Parameters: F_N=-0.7 nN, excitation=200 mV. (c)+(d) Forward and backward scan of a 700 x 700 nm^2 region with higher coverage (>2 ML). Parameters: F_N=2.3 nN, excitation=10 mV. (e)+(f) Forward and backward scan of a 700 x 700 nm^2 region. Parameters: F_N=0 nN, excitation=10 mV.*

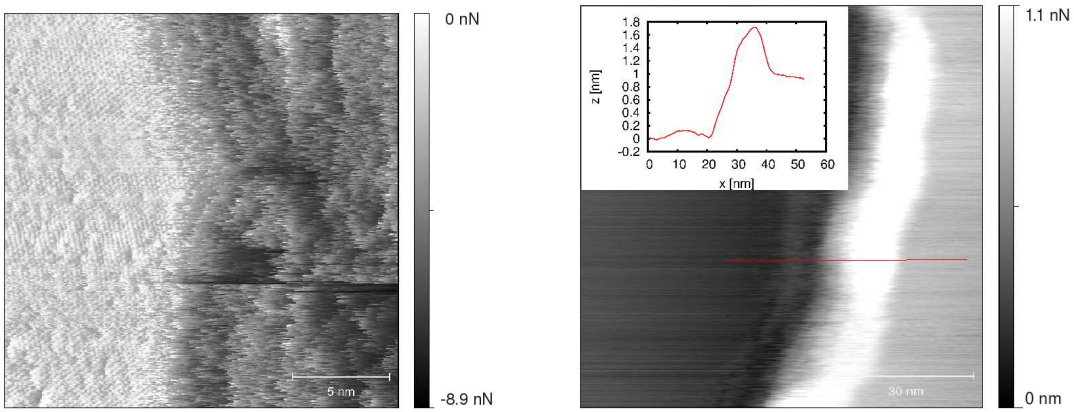

(a) Friction forward (b) Topography

Figure 5.5: *(a) Friction image showing Cu(111) on the left side, while on the right side, the NaCl carpet starts. Compared to the quite acceptable resolution on the copper, the NaCl region does not reveal the atomic lattice. (b) Topography image of another border region, showing the elevation at the edge, probably coming from scratching away material.*

5.2.2 Stick-Slip Measurements

To interpret the large scale scans it is crucial to resolve the atomic lattice of each material, and we were successfull doing this. In this sections, we discuss these measurements taken in constant-height mode, meaning the distance controller was switched off to suppress any additional noise due to wrong gain settings. Since these scans are very small, the normal load is still almost constant, since topographical effects from a tilted sample are negligible. All the scans (and friction loops) in this section have the size of 10 x 10 nm^2. Line sections were always taken along the fast scanning direction.

Cu(111)

As shown in fig. 5.6(a) Cubic stick-slip pattern of NaCl with very little distortion. (b) Friction loop extracted from (a) shows the finite area between forward and backward scan, which corresponds to a non-zero energy loss of about 28.6 eV. (c) Atomic stick slip pattern of Cu(111) revealing the hexagonal crystal lattice. A closer look to the image shows the imprint of the double tip (∼4 nm separated). Nevertheless, the resolution is still very good, since single atomic defects are visible (indicated with the white arrow). Parameters: F_N=5.8 nN and no excitation. (d) Friction loop extracted from (c) clearly shows atomic stick-slip but small energy dissipation, since forward and backward curve almost overlap. All pictures have a size of 10 x 10 nm^2.figure.caption.37, the hexagonal lattice of Cu(111) could be resolved with an almost true atomic resolution (very small defects). After having a closer look at those images, one recognizes that the pattern of defects is doubled, thus a so-called double-tip is the cause of this effect. A double-tip consists of two spatial separated minitips, and both of them contribute to the deflection signal.

Therefore, the AFM images are a convolution of the tip shape and the substrate structure. The nearest-neighbor distance was measured to be ≈ 2.6 $\mathring{A}$, which is in good agreement with the lattice constant of 2.56 $\mathring{A}$. The nature of the impurities can be analyzed by looking at the friction images in fig. 5.6(a) Cubic stick-slip pattern of NaCl with very little distortion. (b) Friction loop extracted from (a) shows the finite area between forward and backward scan, which corresponds to a non-zero energy loss of about 28.6 eV. (c) Atomic stick slip pattern of Cu(111) revealing the hexagonal crystal lattice. A closer look to the image shows the imprint of the double tip (∼4 nm separated). Nevertheless, the resolution is still very good, since single atomic defects are visible (indicated with the white arrow). Parameters: F_N=5.8 nN and no excitation. (d) Friction loop extracted from (c) clearly shows atomic stick-slip but small energy dissipation, since forward and backward curve almost overlap. All pictures have a size of 10 x 10 nm^2.figure.caption.37. As they appear as dark spots, the impurities are facing out of the plane. As reported in [58], the impurities in copper-crystals are mainly sulfur atoms (identifiable by Auger-spectroscopy) diffusing to the surface during the annealing process. To observe if the sulfur atoms are mobile, we made a sequence of 15 images (1 minute each) of the same spot. But we could not identify movement. At the places where the impurities are, the maximal lateral force reaches a value 2-3 times higher than $|F_{L,max}|$ caused by the atomic corrugation of the substrate. The images on Cu(111) were taken at a load of 5.8 nN and no excitation. By extracting profiles through the friction images, it is possible to investigate the stick-slip behavior and energy-dissipation. A friction loop is shown in fig. 5.6(a) Cubic stick-slip pattern of NaCl with very little distortion. (b) Friction loop extracted from (a) shows the finite area between forward and backward scan, which corresponds to a non-zero energy loss of about 28.6 eV. (c) Atomic stick slip pattern of Cu(111) revealing the hexagonal crystal lattice. A closer look to the image shows the imprint of the double tip (∼4 nm separated). Nevertheless, the resolution is still very good, since single atomic defects are visible (indicated with the white arrow). Parameters: F_N=5.8 nN and no excitation. (d) Friction loop extracted from (c) clearly shows atomic stick-slip but small energy dissipation, since forward and backward curve almost overlap. All pictures have a size of 10 x 10 nm^2.figure.caption.37 (b). The forward and backward scan are almost overlapping, therefore the mean friction and thus energy is surprisingly small. The residual friction is $\bar{F_L} \approx 0.049$ nN, and therefore the energy loss in one loop is $\Delta E \approx 4.3$ eV (per slip: ~ 0.065 eV) The average maximal friction force $F_{L,max}$ is around 0.34 nN. These values are much smaller than those reported by the authors in [58].

NaCl

Resolving the atomic structure on alkali-halide crystals is quite easy and has been studied in detail by many authors [2, 28, 25, 24, 23, 56]. The stick-slip pattern shown in fig. 5.6(a) Cubic stick-slip pattern of NaCl with very little distortion. (b) Friction loop extracted from (a) shows the finite area between forward and

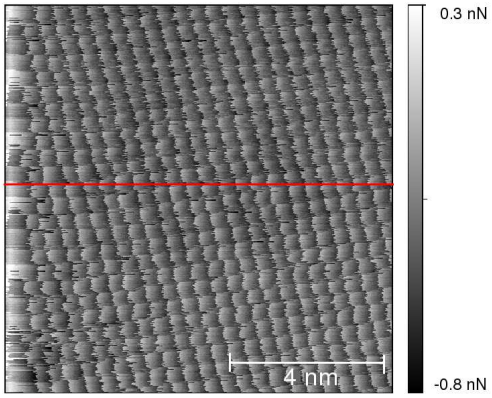

(a) Friction forward

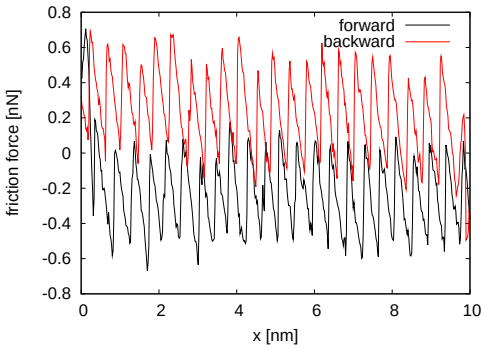

(b) Profile

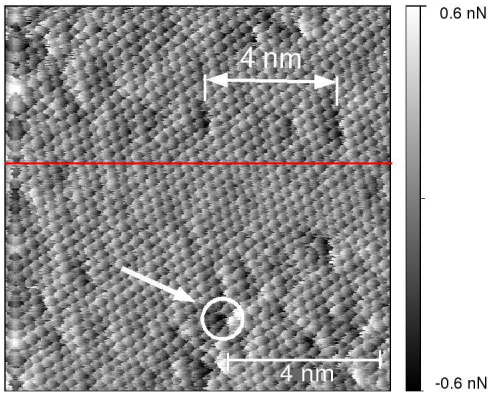

(c) Friction forward

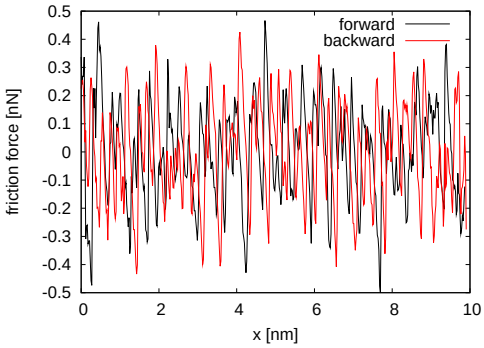

(d) Profile

Figure 5.6: *(a) Cubic stick-slip pattern of NaCl with very little distortion. (b) Friction loop extracted from (a) shows the finite area between forward and backward scan, which corresponds to a non-zero energy loss of about 28.6 eV. (c) Atomic stick slip pattern of Cu(111) revealing the hexagonal crystal lattice. A closer look to the image shows the imprint of the double tip (∼4 nm separated). Nevertheless, the resolution is still very good, since single atomic defects are visible (indicated with the white arrow). Parameters: F_N=5.8 nN and no excitation. (d) Friction loop extracted from (c) clearly shows atomic stick-slip but small energy dissipation, since forward and backward curve almost overlap. All pictures have a size of 10 x 10 nm^2.*

backward scan, which corresponds to a non-zero energy loss of about 28.6 eV. (c) Atomic stick slip pattern of Cu(111) revealing the hexagonal crystal lattice. A closer look to the image shows the imprint of the double tip (∼4 nm separated). Nevertheless, the resolution is still very good, since single atomic defects are visible (indicated with the white arrow). Parameters: F_N=5.8 nN and no excitation. (d) Friction loop extracted from (c) clearly shows atomic stick-slip but small energy dissipation, since forward and backward curve almost overlap. All pictures have a size of 10 x 10 nm^2.figure.caption.37 (c) reveals the cubic lattice with a surface periodicity of a=4.1 $\mathring{A}$ in direction of the atomic rows, the 3D lattice constant found in literature is a_0= 5.65 $\mathring{A}$. This is in good agreement, since one excpect in contact-AFM (as well as nc-AFM), that only one ion species is imaged (if using low loads). Which one depends on the contamination of the tip (Na^+ or Cl^- contaminated): When tip and substrate ion are of the same species, then this corresponds to a strong repulsion (corrugation maximum), if not then they attract each other (corrugation minimum). This picture seems only to be true if the normal load is small and therefore the electrostatic force dominates (sketched in fig. 5.7(a) Under the assumption that only one ionic species is imaged in contact AFM (here e.g. the blue one), the unit cell is rotated by 45^o and the distance between nearest neighbours is reduced by a factor of $\sqrt{2}$. (b) A profile over a sulfur impurity within Cu(111). The maximal friction force reaches about three times its normal value, followed by a enhanced positive friction force after jumping over the impurity.figure.caption.39) (a). If using higher loads, the sitation may change due to the repulsiv forces that are independent of the ionic charge. If we assume that only one ionic species is imaged, then a_0=$a \times \sqrt{2}$=5.79 $\mathring{A}$, which is not far away from the literature value.

Defects on the structure are less pronounced than on Cu(111), however, small distortions on a longer scale are visible. Probably they occur from the underlying sulfur impurities, or they are a weak sign of a superstructure on the NaCl film (strain in the lattice of the bi-layer). Although no evidence for such a superstructure was found during our contact measurements, other authors did [63]. A superstructure is a long range distortion in the film arising from the interaction with the substrate lattice (interference between the two lattice constants). The friction scans on the NaCl films were taken at -1.2 nN load and 20 mV excitation. In contrast to the Cu(111) friction loop, the residual friction is higher on NaCl. We found an average friction force of ≈ 0.27 nN, giving rise to an energy loss of 28.6 eV per loop (0.74 eV per slip). In average, F_{max} is about 0.50 nN. These values are also rather low compared to those of [28] which are 1.4 eV per slip. This can probably be explained by the low load and the use of an excited cantilever.

5.3 Lateral Contact Stiffness

When looking at typical atomic stick-slip curves, the striking thing is that the slope of the sticking part (which represents a spring constant) is much lower than the torsional stiffness of the cantilever [64]. In other words, the weak stiffness of

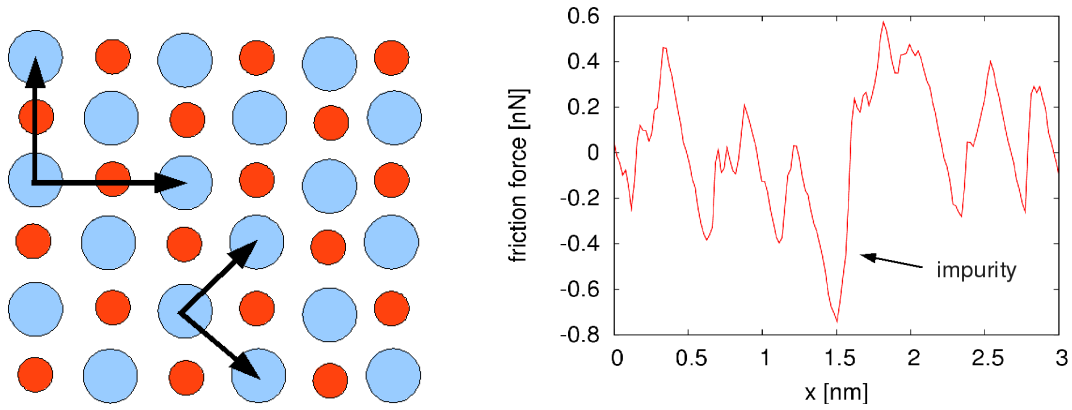

(a) (b)

Figure 5.7: *(a) Under the assumption that only one ionic species is imaged in contact AFM (here e.g. the blue one), the unit cell is rotated by 45° and the distance between nearest neighbours is reduced by a factor of $\sqrt{2}$. (b) A profile over a sulfur impurity within Cu(111). The maximal friction force reaches about three times its normal value, followed by a enhanced positive friction force after jumping over the impurity.*

the contact is mainly dominated by something else than the cantilever, e.g. the deformation of the tip apex or the substrate atoms. Since the springs can be considered to be in a series, the experimental measured lateral stiffness k_{exp} can be expressed as:

$$\frac{1}{k_{exp}} = \frac{1}{k_T} + \frac{1}{k_{tip}} + \frac{1}{k_{surf}} = \frac{1}{k_T} + \frac{1}{\kappa} \quad , \tag{5.1}$$

Where k_{tip} the stiffness of the tip apex and k_{surf} the lateral stiffness of the surface itself. Since it is difficult to separate these two springs, they are together called lateral contact stiffness κ. Typical experiments with sharp tips results in a k_{exp} of 0.5-5 N/m, which is one to two orders of magnitude softer than k_T. If one wants to compare with the Tomlinson model, a further transformation has to be made. The so-called effective lateral stiffness k_{eff} which goes into the relations in section 2.2.1Tomlinson Modelsubsubsection.2.2.1 (for simplicity, k_{eff} is just called k in the Tomlinson model) calculates like [23]

$$k_{eff} = \frac{\eta + 1}{\eta} k_{exp} \tag{5.2}$$

with η from eq. (2.8Tomlinson Modelequation.2.8). Since the prefactor in (5.2Lateral Contact Stiffne exceeds unity, $k > k_{exp}$. In order to make some statistics, over 50 sticking parts have been fitted (for each material). The result is presented in fig. 5.8(a) Measured experimental lateral contact stiffness on both Cu(111) and NaCl. A significant difference is revealed when making a histogram of the 100 fitted sticking-slopes which is then fitted with a Gaussian distribution. For Cu(111) k_{exp}=2.96 ± 0.24 N/m, while for NaCl k_{exp}=1.87 ± 0.17 N/m was determined. (b) Finite element simulation of the deformation of the tip and its apex (magnified) due to a static lateral

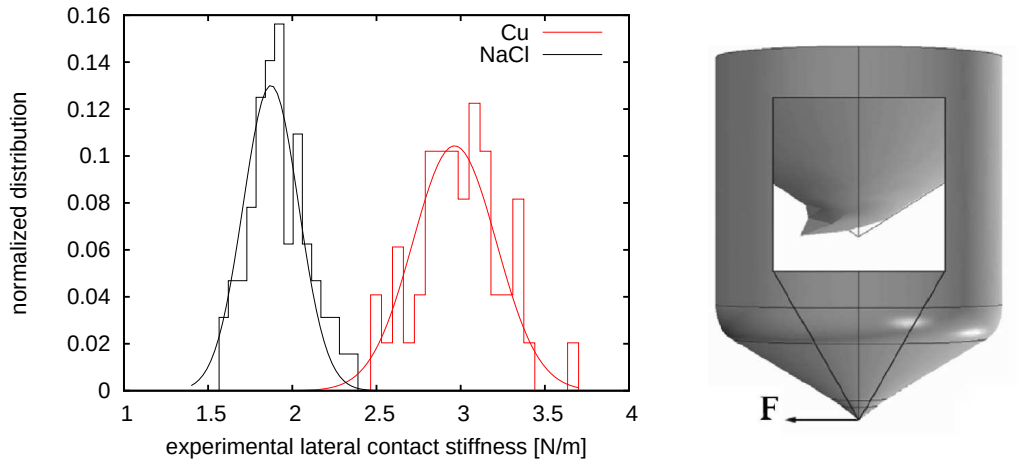

(a) (b)

Figure 5.8: *(a) Measured experimental lateral contact stiffness on both Cu(111) and NaCl. A significant difference is revealed when making a histogram of the 100 fitted sticking-slopes which is then fitted with a Gaussian distribution. For Cu(111) k_{exp}=2.96 ± 0.24 N/m, while for NaCl k_{exp}=1.87 ± 0.17 N/m was determined. (b) Finite element simulation of the deformation of the tip and its apex (magnified) due to a static lateral force. It can bee seen that in a first approximation, only the tip-apex deforms (taken from [64])*

force. It can bee seen that in a first approximation, only the tip-apex deforms (taken from [64])figure.caption.40. It can be shown [65] that η can also be determined out of experimental observables, without directly knowing E_0 which is part of eq. (2.8Tomlinson Modelequation.2.8):

$$\eta = \frac{2\pi F_L^{max}}{k_{exp} a} - 1 \quad . \tag{5.3}$$

Due to thermal effects in experiments at room temperature, F_{max} comes out approximately 25 % too small (since jumps occur earlier), compared to the T=0 K Tomlinson model. In our measurements, we found for Cu(111) k_{exp}=2.96 ± 0.24 N/m, while for NaCl k_{exp}=1.87 ± 0.17 N/m. Calculating η with (5.3Lateral Contact Stiffnessequation gives about the same value for both materials (3.38 ± 0.58 for NaCl, 3.09 ± 1.12 for Cu(111)). The effective lateral stiffness then becomes (without adding 25 % to F_{max}): k_{eff}=3.92 ± 0.44 N/m for Cu(111) and k_{eff}=2.43 ± 0.22 N/m for NaCl. The elastic properties of (cantilever-) tips have been studied in the last few years, especially to understand what is really measured in FFM. Using the finite element method, Lantz et. al [66] found a value for k_{tip}=84 N/m for a sharp silicon cantilever tip, but strongly increasing if the tip is flat (blunt). Recently, other authors claim that the main contribution comes only from the lowest few atoms [64], thus giving rise to a even smaller spring constant of about 1-10 N/m. Since the tip-apex is normally covered with the samples material, our results can be explained qualitatively in both cases by the elastic properties of the material: The shear modulus G of bulk Cu(111) is 14.5 GPa, while for bulk NaCl G=12.6 GPa.

The fact that the contact is so soft implies that a very small region is involved in the deformation. If taking into account only the foremost 10^5 tip atoms being responsible for the lateral deformation, the resulting oscillation frequency of the tip-apex is $f_{tip} = \sqrt{\frac{k}{m}} \approx$ several GHz. This value depends strongly on the mass of the tip, and this is very difficult to quantify, since the resonance frequency and thus its mass have never been measured experimentally. The problem hereby is the limitation of the detection bandwidth (in our system 3 MHz), therefore all signals faster than 3 MHz are invisible for the electronics.

5.4 Contact Dynamics

In the context of contact dynamics, the dynamics of the tip-sample interaction is investigated. One example would be to measure the oscillation frequency of the tip-apex in the potential well after slipping (not yet done). The dynamics of the torsional modes has already been investigated [67]. In this work, we studied the the vertical resonance frequency of the cantilever in terms of a clamped-spring coupled model 5.4.3Models to Estimate the Contact Stiffnesssubsubsection.5.4.3. As the "normal contact resonance frequency", we understand the resonance frequency of the first normal vibration mode of the cantilever after snapping into contact. This characteristic frequency is about four times higher than the free one, and depends mainly on the contact/sample properties and the static load 5.4.5Load Dependence of the Contact Resonance Frequencysubsubsection.5.4.5.

5.4.1 Direct Mapping of the Stiffness

The idea to image directly the elastic properties of the substrate was adapted from U. Rabe et al. [14], who developed a technique called atomic force acoustic microscopy (AFAM). There are mainly two approaches to probe the properties of the sample, either one excites to cantilever at a fixed frequency and then investigates its amplitude, or the resonance frequency is directly tracked electronically. The first technique gives only a qualitative material contrast. Two of such images are shown in fig. 5.9(a) Topography image of 127 x 127 nm ^{2}. (b) Same image but now the amplitude is mapped (without units). On the Cu(111), the amplitude is higher than on the NaCl. (c) 700 x 700 nm ^{2} topography image. (d) Amplitude channel of (c), again the copper appears brighter. Image parameters: (a)+(b)excitation 200 mV, F_N=-0.73 nN, f_{exc}= 55.24 kHz (c)+(d) excitation 60 mV, F_N=1.5 nN, f_{exc}= 56.22 kHz.figure.caption.41 (b)+(d). The material contrast is clearly visible, since the copper (bright) gives a higher response than the salt films (dark). The calibration of the oscillation amplitude is different in contact and of a free cantilever, because the deflection signal is in a first approximation only given by the change of the cantilevers angle and not its vertical displacement. As can be seen in section 5.4.3Models to Estimate the Contact Stiffnesssubsubsection.5.4.3, the sample stiffness is not know very accurate, and therefore an accurate amplitude calibration is not possible. However, it is at least possible to calibrate the force

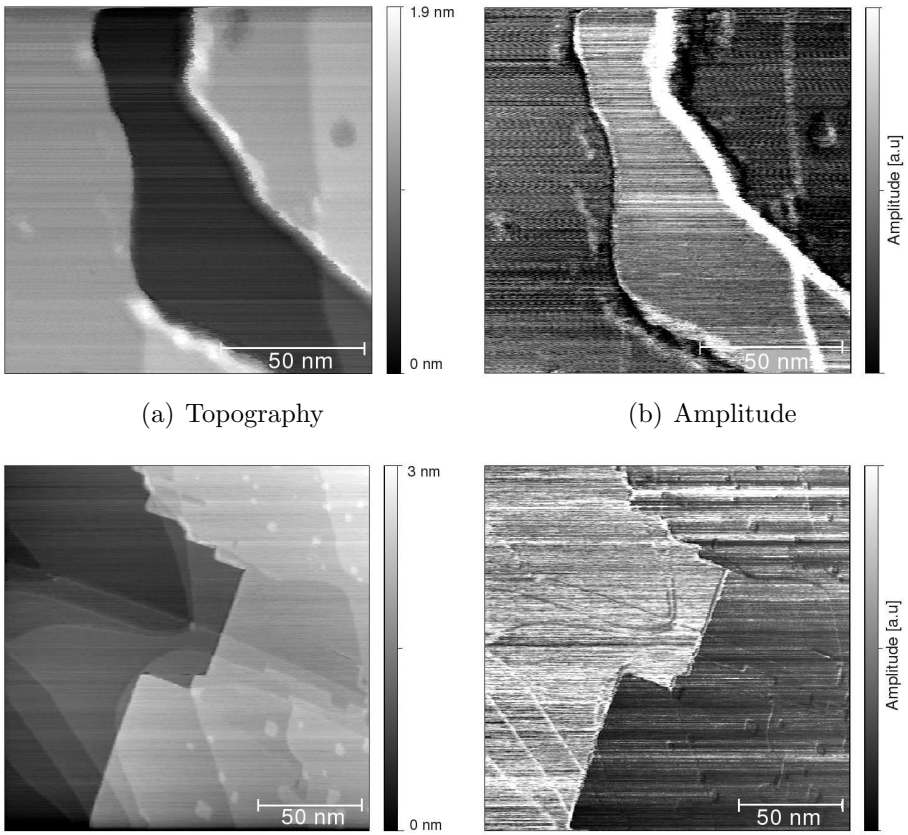

(a) Topography (b) Amplitude

(c) Topography (d) Amplitude

Figure 5.9: *(a) Topography image of 127 x 127 nm ^{2}. (b) Same image but now the amplitude is mapped (without units). On the Cu(111), the amplitude is higher than on the NaCl. (c) 700 x 700 nm ^{2} topography image. (d) Amplitude channel of (c), again the copper appears brighter. Image parameters: (a)+(b)excitation 200 mV, F_N=-0.73 nN, f_{exc}= 55.24 kHz (c)+(d) excitation 60 mV, F_N=1.5 nN, f_{exc}= 56.22 kHz.*

acting on the contact (see appendix of [62]). First calculations indicate that the force acting on the sample is much higher than the static load F_N.

The material contrast can be explained by two different mechanism. On one hand, the Cu(111) seems to have a bigger "intrinsic" (material specific) amplitude response as shown in section 5.4.2Local Frequency Spectrasubsubsection.5.4.2. This could be understood by the higher rigidity of Cu(111) and the higher damping of the thin films that may occur because of its weak binding to the substrate (interface friction?). On the other hand, it depends of course on the excitation frequency f_{exc}, since the two surfaces have their amplitude maximum at different frequencies. However, on all the pictures taken in this experiment, the amplitude is higher on copper. An enhanced amplitude response can be observed at Cu/NaCl borders als well as at copper-steps (free ones and buried ones).

The second method in principle works like nc-AFM, where the PLL tracks the resonance frequency of the cantilever continuously, which gives a net frequency

shift in respect to the resonance frequency of the undisturbed oscillating cantilever. However in contact, the resonance frequency is not that well defined as in nc-AFM, since resonance curves are much broader (low Q-factor, thus slower reaction timescales) and the tip-sample forces are highly non-linear as shown in fig. 5.11(a) All the 8 recorded resonance curves. (b) Averaged spectra reveal a difference in resonance frequency of 260 Hz. (c) Numerical calculation of a resonance curve. As a consequence of the asymmetry, jump phenomena may occur: The red line indicates a jump if detuning from right to left, the blue line represents a possible jump if detuning from left to the right. The different curves are obtained by using different excitation amplitudes, which strongly influence the bending of the peak. (adapted from [68])figure.caption.43. Therefore it is much more difficult to find suitable controller settings. If succeeded in obtaining stable conditions, a contact resonance frequency map can be produced. This is of course much faster than doing e.g. a local frequency sweep on a grid. Such images are shown in fig. 5.10(a)+(c)+(e) Measurements of a 600 x 600 nm^2 area. On the left side and at the top right corner there is the salt, the darker area in the topographic image is the Cu(111) substrate. Map of contact resonance frequencies (=frequency shift + f_0.) is shown in the 2^{nd} row. In an average, the frequency is 255 Hz higher on Cu(111) compared with the thin salt film, as shown in the profile. (b)+(d)+(f) Images of a 2^{nd} layer island with a height of 2.8 $\mathring{A}$. The frequency image in the 2^{nd} row shows an average frequency shift between the bi-layer and the 2^{nd} layer of 50-100 Hz as shown in. Parameters: (a)+(c) excitation 40 mV, F_N=0 nN, (b)+(d) amplitude controlled, F_N=0 nN.figure.caption.42 (c)+(d). By comparing the contact resonance image with the topography and friction channel, it is easy to see the material contrast. Although there are a lot of instabilities (tip changes etc.), it can be still seen that the average frequency on the Cu(111) is higher than the one on the NaCl film. A profile over the material border (averaged over 10 horizontal lines) fitted with a step-function reveals a difference in frequency of 255 Hz. Figures 5.10(a)+(c)+(e) Measurements of a 600 x 600 nm^2 area. On the left side and at the top right corner there is the salt, the darker area in the topographic image is the Cu(111) substrate. Map of contact resonance frequencies (=frequency shift + f_0.) is shown in the 2^{nd} row. In an average, the frequency is 255 Hz higher on Cu(111) compared with the thin salt film, as shown in the profile. (b)+(d)+(f) Images of a 2^{nd} layer island with a height of 2.8 $\mathring{A}$. The frequency image in the 2^{nd} row shows an average frequency shift between the bi-layer and the 2^{nd} layer of 50-100 Hz as shown in. Parameters: (a)+(c) excitation 40 mV, F_N=0 nN, (b)+(d) amplitude controlled, F_N=0 nN.figure.caption.42 (c)+(d) are showing the resonance frequency map of a small 2^{nd} layer island. By taken a profile over the island and averaging over 40 horizontal lines, a frequency-shift of around 50-100 Hz is revealed (lower frequency at the islands). This can be explained by the lower intrinsic stiffness of NaCl: The higher the islands, the less is the influence of the underlying (harder) Cu(111) and the more behaves the salt film like bulk NaCl. But for a clear answer, the resonance frequency for bulk NaCl should be measured with the same cantilever and tip conditions.

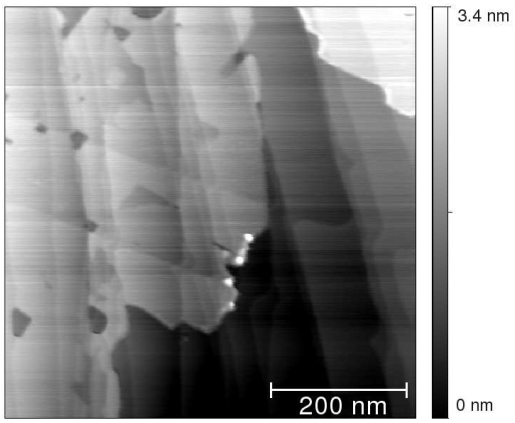

(a) Topography

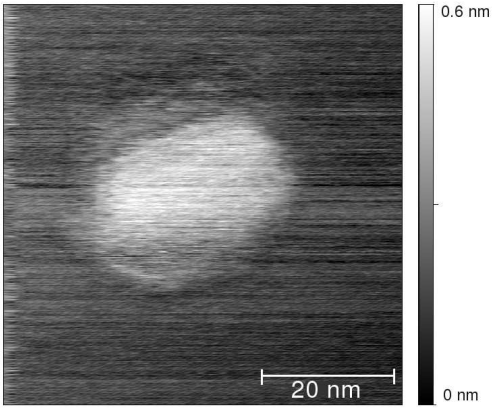

(b) Topography

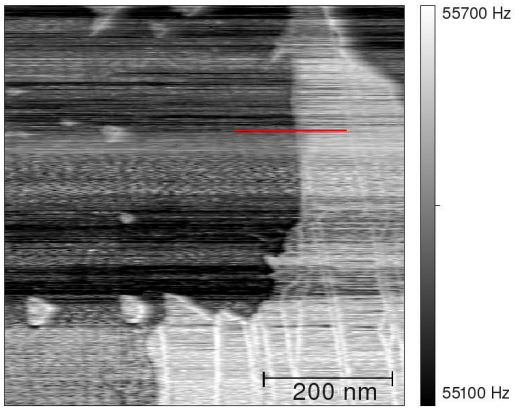

(c) Frequency (shift)

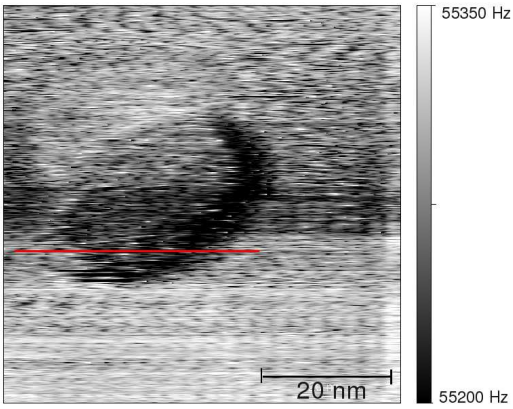

(d) Frequency (shift)

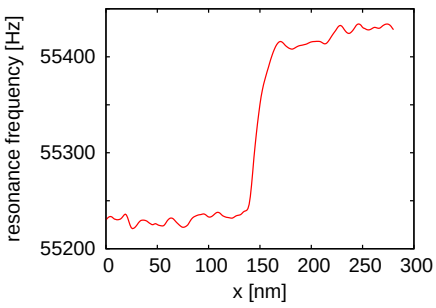

(e) Profile

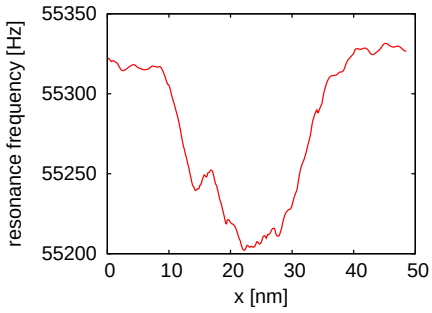

(f) Profile

Figure 5.10: *(a)+(c)+(e) Measurements of a 600 x 600 nm^2 area. On the left side and at the top right corner there is the salt, the darker area in the topographic image is the Cu(111) substrate. Map of contact resonance frequencies (=frequency shift + f_0.) is shown in the 2nd row. In an average, the frequency is 255 Hz higher on Cu(111) compared with the thin salt film, as shown in the profile. (b)+(d)+(f) Images of a 2nd layer island with a height of 2.8 Å. The frequency image in the 2nd row shows an average frequency shift between the bi-layer and the 2nd layer of 50-100 Hz as shown in. Parameters: (a)+(c) excitation 40 mV, F_N=0 nN, (b)+(d) amplitude controlled, F_N=0 nN.*

5.4.2 Local Frequency Spectra

To confirm the different resonance frequencies obtained in the last section, frequency-sweeps have been done both on the first NaCl layer and on the bulk Cu(111) with a constant excitation of 50 mV, in direction from lower frequency to higher ones. The experiment has been repeated four times each. Since the resonance curves are quite reproducible, they have been averaged in fig. 5.11(a) All the 8 recorded resonance curves. (b) Averaged spectra reveal a difference in resonance frequency of 260 Hz. (c) Numerical calculation of a resonance curve. As a consequence of the asymmetry, jump phenomena may occur: The red line indicates a jump if detuning from right to left, the blue line represents a possible jump if detuning from left to the right. The different curves are obtained by using different excitation amplitudes, which strongly influence the bending of the peak. (adapted from [68])figure.caption.43. A resonance frequency of 55'510 Hz was measured for Cu(111) and 55'260 Hz for NaCl. Therefore, the two peaks are separated by a frequency $\Delta f_{res} \approx 260$ Hz from each other. The Q-factor was estimated to be in the order of 1000 for Cu(111) and less than 30 for the NaCl film. In contrast to a model resonance curve produced e.g. by a driven oscillator:

$$A(f) = \frac{A_0}{\sqrt{(1 - \frac{f}{f_0}^2)^2 + \frac{f}{f_0 Q}^2}} \tag{5.4}$$

the contact resonance curves are much more asymmetric with a steep ascent on the left side of the peak and a smooth decay on its right side. This is a consequence of the non-linear potential of the contact. The non-linearity bends the curve to the left, the more the stronger the excitation is. That means in other words that the resonance frequency is a function of the excitation strength and therefore the amplitude. As indicated in fig. 5.11(a) All the 8 recorded resonance curves. (b) Averaged spectra reveal a difference in resonance frequency of 260 Hz. (c) Numerical calculation of a resonance curve. As a consequence of the asymmetry, jump phenomena may occur: The red line indicates a jump if detuning from right to left, the blue line represents a possible jump if detuning from left to the right. The different curves are obtained by using different excitation amplitudes, which strongly influence the bending of the peak. (adapted from [68])figure.caption.43 (c) the bending of the frequency-response curves leads to multivalued amplitudes and hence to jump phenomena [68, 69]. These jumps then leads to a steep left side of the spectra.

On the left side of the Cu-peak a small side resonance can be seen exactly at the NaCl-resonance frequency. A meaningful explanation for this phenomenon could not be found at this time. Probably it comes from the NaCl-covered tip, whose atoms still have their own resonance frequency which overlaps with the main resonance from the sample.

In all the experiments from this and the last chapter, it is not really known how far the properties of the films differ from bulk NaCl crystals. Therefore, it is

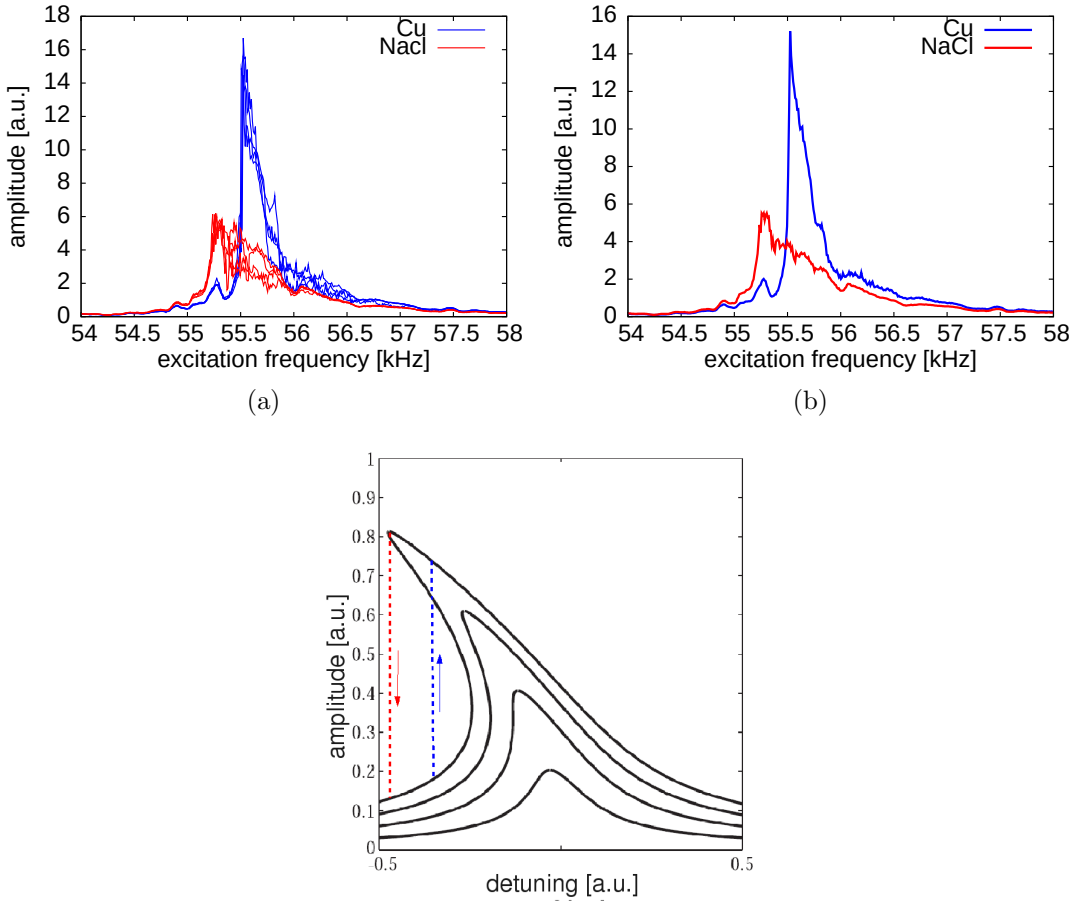

Figure 5.11: *(a) All the 8 recorded resonance curves. (b) Averaged spectra reveal a difference in resonance frequency of 260 Hz. (c) Numerical calculation of a resonance curve. As a consequence of the asymmetry, jump phenomena may occur: The red line indicates a jump if detuning from right to left, the blue line represents a possible jump if detuning from left to the right. The different curves are obtained by using different excitation amplitudes, which strongly influence the bending of the peak. (adapted from [68])*

difficult to determine if the presented results give information about the material "NaCl" or if they are only characteristic for thin films.

5.4.3 Models to Estimate the Contact Stiffness

Models to interpret the contact resonances and to make a link to the elastic properties of the sample are (almost) all based on so-called it characteristic equations. Only wavenumbers k_n (n=1,2,...) that fulfill the characteristic equation of a system, can be a solution of the beam-equation (flexural-theory, which is a differential equation of 4^{th} order [52]:

$$EI\frac{\partial^4 y}{\partial x^4} + \rho A\frac{\partial^2 y}{\partial t^2} = 0 \qquad , \tag{5.5}$$

where E is the Young's modulus, I the moment of inertia, A the cross section and $y(x,t)$ the deflection of the cantilever. The function $y(x,t)$ is also called shape-function, since it represents the actual shape of the cantilever. The characteristic equation for the clamped-free cantilever is e.g.:

$$cos(k_n L)cosh(k_n L) + 1 = 0 \qquad . \tag{5.6}$$

The quantity $k_n L$ is called normalized wavenumber, where L is the length of the cantilever. From the solution of this equations, the free resonance frequency of the n'the eigenmode is then given by

$$f_{n,free} = \frac{(k_n L)^2}{c_c^2} \qquad , \tag{5.7}$$

where c_c is a material constant containing geometrical information and material constants of the cantilever. The wavenumber in contact $k_{n,cont}$ can be either calculated via eq. (5.10Point Mass Modelequation.5.10) or easier by using the relation [31]

$$k_{n,cont}L = k_{n,free}L \times \sqrt{\frac{f_{n,cont}}{f_{n,free}}} \qquad . \tag{5.8}$$

We know $k_{n,free}L$ from the solutions of the equation (5.6Models to Estimate the Contact Stiffnessequ (e.g. $k_{1,free}L$=1.875). Since the free resonance frequency $f_{n,free}$ and the contact resonance frequency $f_{n,cont}$ can be measured directly , we did not have to use (uncertain) input values. For the spectra of section 5.4.2Local Frequency Spectrasubsubsection.5.4.2, we end up with $k_{1,cont}L$=4.151 for copper and 4.141 for the NaCl film. From now on, we call $k_{n,cont}$ simply k_n, since we are only intressted in the contact dynamic.

In the following, several methods are presented to calculate the normal contact stiffness out of a measured contact resonance frequency:

Point Mass Model

This model, originally used for nc-AFM and other oscillator-problems does not make use of a characteristic equation. Instead, it approximates the cantilever by one spring and one (point) mass. As we know from the normal harmonic oscillator, the square of the eigenfrequency is given by k/m. Since The cantilever is not a point mass, one has to define an effective mass m^* of the cantilever, which is $\approx \frac{1}{4}$ of the real mass. Then the resonance frequency can immediately be calculated with

$$\omega_{1,free} = \sqrt{\frac{k_N}{m^*}} \quad . \tag{5.9}$$

When going into contact, second spring k^* has to be introduced which represents the contact stiffness. Therefore, we replace k_N with an effectiv spring constant $k_N + k^*$. Using this property and solving the equation for k^* we end up with

$$k^* = k_N \left[\left(\frac{f_{1,cont}}{f_{1,free}} \right)^2 - 1 \right] \quad . \tag{5.10}$$

Inserting the numbers gives a stiffness of 2.46 N/m for copper and 2.44 N/m for NaCl respectively. This results are quite comparable with the lateral stiffness (which is 1.87 N/m for NaCl and 2.96 N/m for Cu(111), respectively), but it has been shown [70] that the point mass model fails to predict the contact stiffness in the case of $k^* \gg k_N$, and this seems to be the case in our case (see below). The main problem is the evaluation of m*: Since its value was determined for a free cantilever, the application for (almost) pinned tips seems doubtful because of the different dynamic.

Model A

A model that treats this problem in a more specific way is based on the characteristic equation of the clamped-spring-coupled cantilever. There are three characteristic length as model parameters, as sketched in fig. 5.12(a) Sketch of the cantilever-surface-coupled model used to derive eq. (5.11Model Aequation.5.11). (b) Band structure obtained by analytical evaluation of eq. (5.12Model Aequation.5.12). for n=1,2,3. For the gray regions, there exist no solution and therefore, wavenumbers in this region cannot be evaluated. (c) SEM picture of a contact-cantilever of the same wafer us the original one. (d) Numerical evaluation of eq. (5.11Model Aequation.5.11) as a function of $k_n L$ and the ratio L_1/L. The strong influence of the tip position can be seen, since the curve shifts to the right for smaller L_1/L. (a) and (b) taken from [71].figure.caption.46: L_1 is the length from the chip to the tip, L' the length from the tip to the end and $L = L_1 + L'$ is the total length. The calculation is done similar to the free case, but eq.(5.5Models to Estimate the Contact Stiffnessequation.5.5) has to be modified with an additional force -$k^* \cdot y$ coming from the contact. For

a detailed derivation of these expressions, see the appendix of [71]. Using suitable boundary conditions for the spring-coupled end, the characteristic equation then reads:

$$\begin{aligned} & (coshk_nL_1sink_nL_1 - sinhk_nL_1cosk_nL_1) \\ \times \quad & (1 + cosk_nL'coshk_nL') \\ - \quad & (coshk_nL'sink_nL' - sinhk_nL'cosk_nL') \\ \times \quad & (1 - cosk_nL_1coshk_nL_1) \\ = \quad & -2k_n^3\frac{EI}{k^*}(1 + cosk_nLcoshk_nL) \end{aligned} \tag{5.11}$$

For L'=0, this model simplifies to:

$$sinhk_nLcosk_nL - coshk_nLsink_nL = \frac{(k_nL)^3k_N}{3k^*}(1 + cosk_nL - coshk_nL) \tag{5.12}$$

where k_N is the stiffness of the free cantilever. This model delivers nice band-structure-like results, as shown in fig. 5.12(a) Sketch of the cantilever-surface-coupled model used to derive eq. (5.11Model Aequation.5.11). (b) Band structure obtained by analytical evaluation of eq. (5.12Model Aequation.5.12). for n=1,2,3. For the gray regions, there exist no solution and therefore, wavenumbers in this region cannot be evaluated. (c) SEM picture of a contact-cantilever of the same wafer us the original one. (d) Numerical evaluation of eq. (5.11Model Aequation.5.11) as a function of k_nL and the ratio L_1/L. The strong influence of the tip position can be seen, since the curve shifts to the right for smaller L_1/L. (a) and (b) taken from [71].figure.caption.46. But there are also gaps in the space of possible solutions for k^* for a given k_nL, thus resulting in a non-physical result (e.g. negative). Solving eq. (5.12Model Aequation.5.12) for k^* gives no solution for our values of k_nL, since k_nL=3.92 is already the solution for k* = ∞. As also admitted by the authors of the mentioned paper, eq. (5.12Model Aequation.5.12) delivers not suitable results in most of the cases. The more general eq. (5.11Model Aequation.5.11) is able to shift the "border" k* = ∞ to higher k_nL by considering the influence of the tip position, as plotted in fig.5.12(a) Sketch of the cantilever-surface-coupled model used to derive eq. (5.11Model Aequation.5.11). (b) Band structure obtained by analytical evaluation of eq. (5.12Model Aequation.5.12). for n=1,2,3. For the gray regions, there exist no solution and therefore, wavenumbers in this region cannot be evaluated. (c) SEM picture of a contact-cantilever of the same wafer us the original one. (d) Numerical evaluation of eq. (5.11Model Aequation.5.11) as a function of k_nL and the ratio L_1/L. The strong influence of the tip position can be seen, since the curve shifts to the right for smaller L_1/L. (a) and (b) taken from [71].figure.caption.46 (c). The strong influence of L' can be understood by the fact that in the free case the oscillation is only given (despite tip mass) by the total length L, yet in contact L' is the characteristic length of the cantilever and therefore resulting in a smaller wavenumber. Considering the values for k_nL, there is (as expected) no solution for eq. (5.11Model Aequation.5.11). For eq.

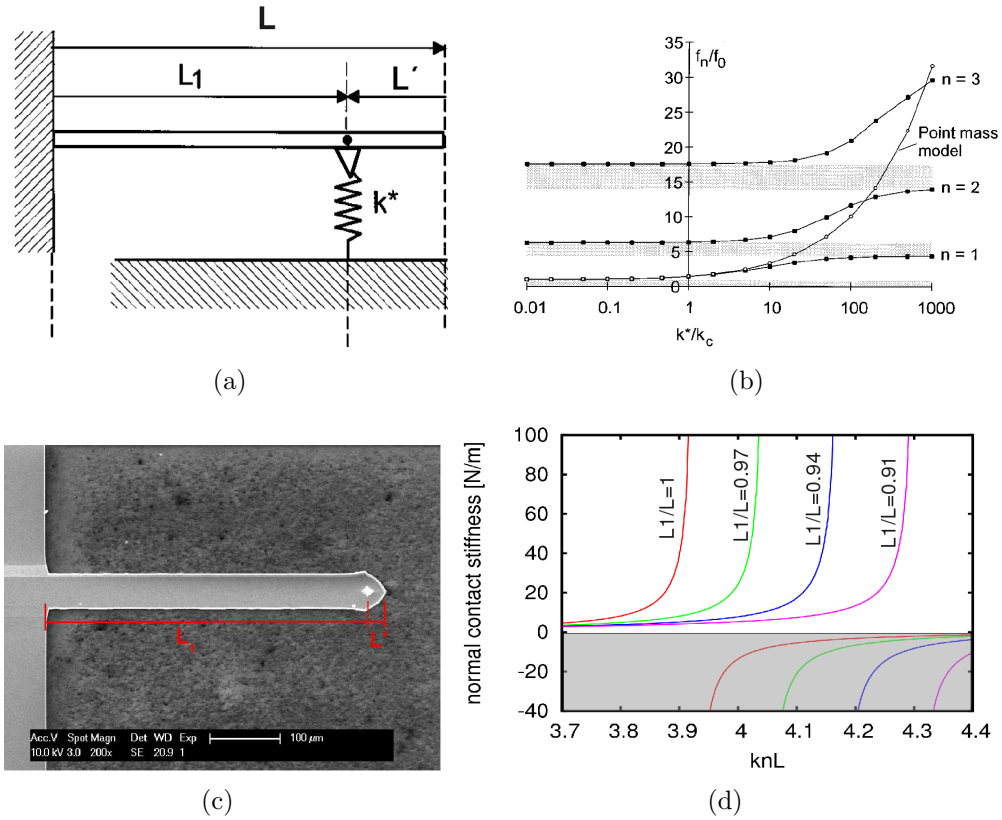

Figure 5.12: *(a) Sketch of the cantilever-surface-coupled model used to derive eq.* (5.11Model Aequation.5.11). *(b) Band structure obtained by analytical evaluation of eq.* (5.12Model Aequation.5.12). *for n=1,2,3. For the gray regions, there exist no solution and therefore, wavenumbers in this region cannot be evaluated. (c) SEM picture of a contact-cantilever of the same wafer us the original one. (d) Numerical evaluation of eq.* (5.11Model Aequation.5.11) *as a function of k_nL and the ratio L_1/L. The strong influence of the tip position can be seen, since the curve shifts to the right for smaller L_1/L. (a) and (b) taken from [71].*

(5.12Model Aequation.5.12), using L_1/L=0.95 from SEM-pictures, the solutions are also negative (but less "far" away from a solution).

Model B

The model in this paragraph is a further extension of the model discussed above. The main idea is the consideration of a tilt-angle ϵ between cantilever and sample, thus resulting in a crosstalk between normal- (k^*) and lateral contact-stiffness κ. As shown in section 5.3Lateral Contact Stiffnesssubsection.5.3, the lateral contact contact stiffness is in the order of 2 N/m. If the normal stiffness is higher than the lateral, then a tilt would lead to an apparent reduced k^* and thus to a lower resonance frequency. In other words, the possible solutions of k^* are shifted further to the right (to higher k_nL, higher $f_{1,cont}$). The quantitative evaluation of such a crosstalk is given in [32, 72, 31], where the (quite complicated) equations are derived. In a form that lends itself to a numerical solution, the normal contact stiffness can then be written as

$$k^* = k_N \times \frac{-B + \sqrt{B^2 - 4AC}}{6A} \quad . \tag{5.13}$$

The functions A, B and C are given by

$$\begin{aligned} A &= \left(\frac{\kappa}{k^*}\right)\left(\frac{h}{L_1}\right)^2 (1 - cosk_nL_1 coshk_nL_1) \\ &\times \quad (1 + cosk_nL_1' coshk_nL') \\ \\ B &= B_1 + B_2 + B_3 \\ \\ C &= 2(k_nL_1)^4(1 + cosk_nL_1 coshk_nL) \quad . \end{aligned}$$

The terms B_{1-3} which are a function of ϵ and $\frac{\kappa}{k^*}$ are given in A.4Terms B_1, B_2, B_3subsection.A.4. In our AFM, the angle ϵ=13° is given by the cantilever-holder (Ti-block), on which the chip is glued. So there are six independent input-parameters for eq. (5.15Model Bequation.5.15): L_1, L', ϵ, h, κ and of course k_N. The strongest influence on k^* are given by L' and h (see fig. 5.13(a) Sketch of model B, taken from [32]. (b) Dependencies of eq. (5.15Model Bequation.5.15): Strong influence of L' and tip height (leaving all other parameters constant). (c) Crosstalk only plays a roll when $\kappa \ll k^*$.figure.caption.48). The fact that A and B_{1-3} contain also $\frac{\kappa}{k^*}$ does not allow a direct evaluation of k^*. Instead, a self consistent $\frac{\kappa}{k^*}$ has to be found. This value is given e.g. by the point $x=\frac{\kappa}{k^*}$ where

$$\frac{\kappa}{k^*\,(k_nL, x)}/x = 1 \qquad \text{is fullfilled} \quad . \tag{5.14}$$

This value can then be used as an input for eq. (5.15Model Bequation.5.15). The value for κ can be obtained experimentally as shown in section 5.3Lateral Contact

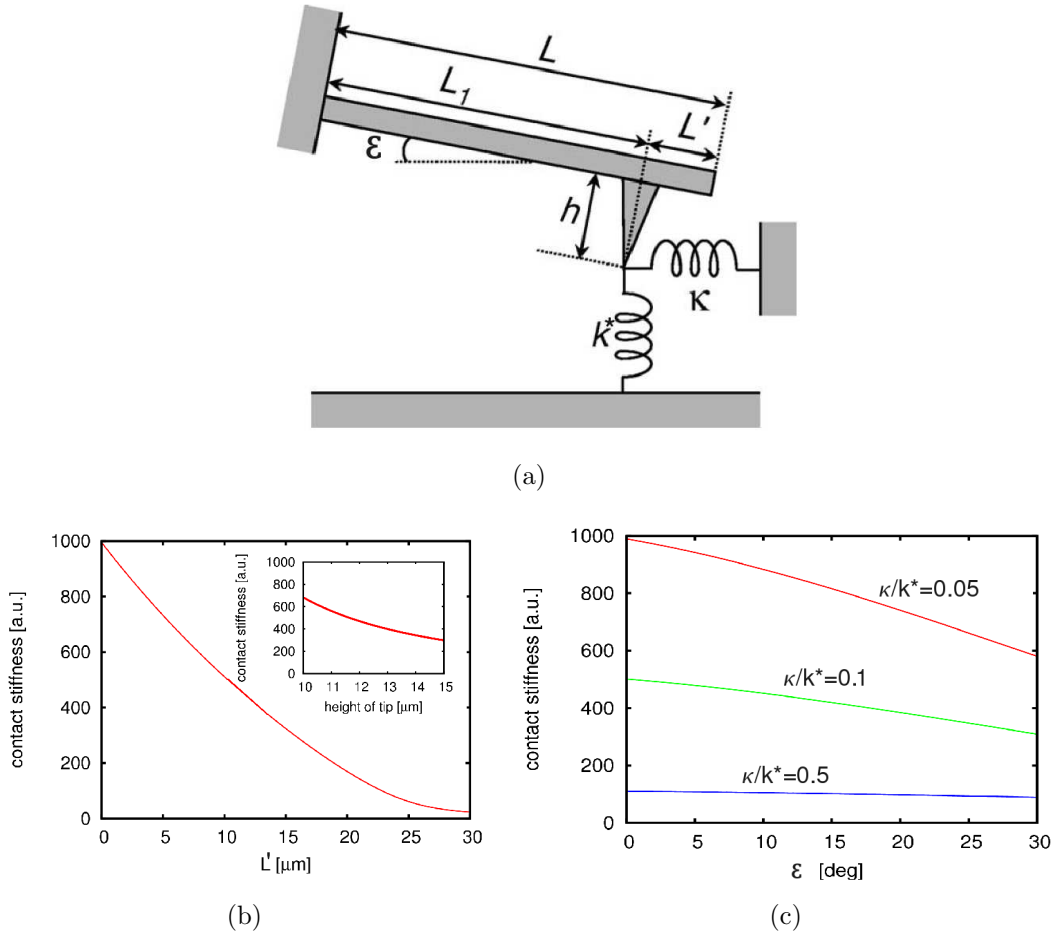

Figure 5.13: *(a) Sketch of model B, taken from [32]. (b) Dependencies of eq.* (5.15Model Bequation.5.15)*: Strong influence of L' and tip height (leaving all other parameters constant). (c) Crosstalk only plays a roll when $\kappa \ll k^*$.*

Stiffnesssubsection.5.3. Since the contact is dominated by the stiffness of the tip and the sample, the influence of the cantilever-stiffness is negligible. So the contact stiffness is approximately given by:

$$\kappa = \left(\frac{1}{k_{exp}} - \frac{1}{k_T} \right)^{-1} \approx k_{exp} \quad . \tag{5.15}$$

Unfortunately, the cantilever used for these contact resonance experiment was not stored for further SEM investigation. For this reason, another cantilever out of the same wafer was taken as a reference. The measurement revealed L_1=451 μm, L'= 24.8μm and h= 12.5μm. The total lenght L is therefore 475.8 μm.

Using these values, one finds for NaCl κ/k^*=0.032 and thus k^*=58.4 N/m, while for Cu(111) κ/k^*=0.033 and k^*=89.7 N/m. It is quite astonishing (but also somehow clear) that the ratio $\kappa_{cu}/\kappa_{NaCl} \approx k^*_{cu}/k^*_{NaCl}$. Estimating an error is not that easy, since already very small changes in e.g. L' makes a huge difference.

	E [GPa]	ν (Poisson ratio)	E^*_{Si-xx} [Gpa]	a_C [nm]
NaCl	39.98	0.25	34.83	0.83
Cu	120	0.34	78.75	0.57
Si	169	0.33		

Table 2: *Material constants for the involved materials. The third column shows the effectiv Young's modulus for the tip-sample system. The fourth column shows an approximative value for the contact radius from eq.* (2.14Hertzian Contact Modelequation.2.14) *and the suitable values for* k^*.

Variating L' by $\pm 2\mu$m, h by $\pm 1\mu$m and ϵ $\pm 4^o$ (those have the biggest influence) gives an strongly asymmetric error-bar. The error given here is the variation of the predicted value for k* by using (5.15Model Bequation.5.15) with the uncertenties given above. We get for NaCl: k^*=58.4 $^{+119}_{-27}$ N/m . For copper the range is k^*=89.7 $^{+\infty}_{-51}$ N/m. Since the error range is much smaller in the negative direction, at least a lower limit can be given: k^* >31 N/m for NaCl and k^* >38 N/m for copper, respectively. Within the Hertz theory, a contact radius can now be calculated using eq. (2.14Hertzian Contact Modelequation.2.14) ($a_C = k^*/2E^*$). Using the effective Young's moduli from table 2Material constants for the involved materials. The third column shows the effectiv Young's modulus for the tip-sample system. The fourth column shows an approximative value for the contact radius from eq. (2.14Hertzian Contact Modelequation.2.14) and the suitable values for k^*.table.caption.49, the calculated contact radius is 0.83 nm for NaCl and 0.57 nm for Cu (again keeping in mind the large errors!). This values are of the order of magnitude of what we excpected: The contact does not consits of a single but around 5-10 atoms.

5.4.4 Higher Harmonics

In order to study the behavior of the first harmonic of the fundamental mode (at 2ω), the cantilever was excited at the contact resonance frequency and then we recorded both amplitudes. We hoped to find some features in those images that are not in the normal amplitude channel, but we could not find any (also due to the coarse digitalization). It is known that higher harmonics contain more information about non-linear tip-sample forces, which is used especially in tappping mode (see e.g. [73, 74]). In our measurements an material contrast inversion from the normal amplitude A_1 to the amplitude of the first harmonic A_2 could be identified. While A_1 is higher on Cu(111) than on NaCl, the opposite is the case for A_2, as shown in fig. 5.14(a) Amplitude of the contact resonance of a 700 x 700 nm region (b) Amplitude of the first harmonic of the same region. The contrast between the two materials is inverted. Image parameters: f_{exc}=55.24 kHz/110.48 kHz, excitation=100 mV, load=-0.2 nN.figure.caption.50. Steps and impurities are enhanced in both channels.

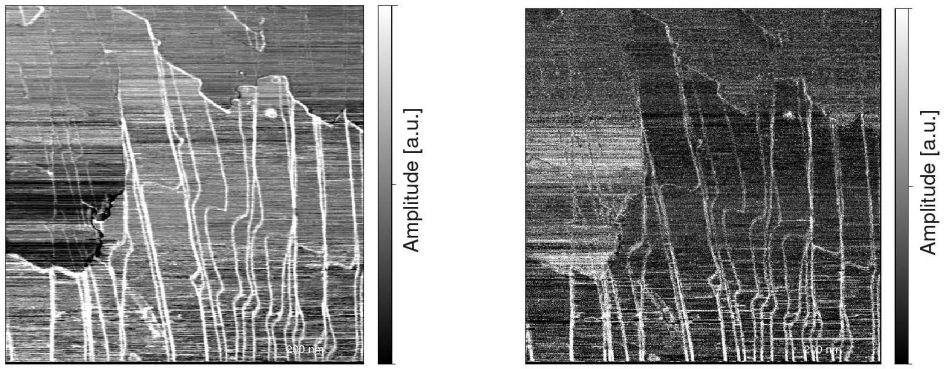

(a) Amplitude 1 (b) Amplitude 2

Figure 5.14: *(a) Amplitude of the contact resonance of a 700 x 700 nm region (b) Amplitude of the first harmonic of the same region. The contrast between the two materials is inverted. Image parameters: f_{exc}=55.24 kHz/110.48 kHz, excitation=100 mV, load=-0.2 nN.*

5.4.5 Load Dependence of the Contact Resonance Frequency

This experiment has been done on a different sample, namely thin KBr-films on Cu(111). The goal was to investigate the contact resonance frequency (of the fundamental mode) in dependence of the static load. A similar experiment has been done with at first torsional mode [24]. It has been found that for sharp tips, the frequency does not change with load. But repeating the same experiment with a round tip resulted in a increasing frequency with higher loads. For the normal vibration mode, one should intuitively expect a higher $f_{n,cont}$ for higher loads, since the contact becomes somehow "stiffer". The experiment has been done with a non-reflex contact-cantilever with $f_{1,free}$=8885 Hz and k_N=0.05 N/m. The thermal noise spectrum has been recorded for 13 different loads. For each load, the spectrum was averaged 20 times in order to reduce the noise. As shown in fig. 5.15(a)+(b) A selection of five thermal noise curves recorded with different static loads. The peaks become broader with higher negative load. The frequency shift is about 390 Hz per 1 nN load increment.figure.caption.51, it has been found that the contact resonance frequency increases slightly with load (390 Hz per 1 nN). Also the Q-factor decreases from ∼1400 for the maximal load to ∼400 for the minimal load. But this behavior is not always reproducible, there are some resonance curves that do not obey this trend. The curves shown in fig. 5.15(a)+(b) A selection of five thermal noise curves recorded with different static loads. The peaks become broader with higher negative load. The frequency shift is about 390 Hz per 1 nN load increment.figure.caption.51 are only a selection of all curves, showing the basic behavior. This result can be understood within the Hertzian model, where the contact area $2\pi a_C$ is a function of the load (see eq. (2.14Hertzian Contact Modelequation.2.14)). Using this relation, one finds

$$k^* \propto a_C \propto F_C^{\frac{1}{3}} \quad , \tag{5.16}$$

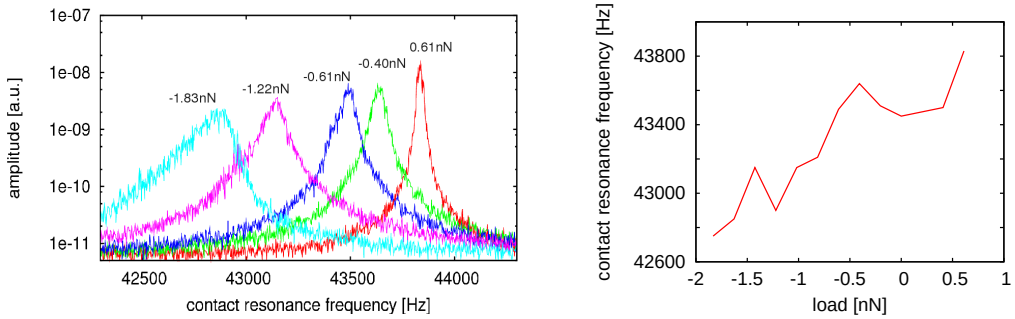

Figure 5.15: *(a)+(b) A selection of five thermal noise curves recorded with different static loads. The peaks become broader with higher negative load. The frequency shift is about 390 Hz per 1 nN load increment.*

and with the models discussed above, the results can be explained quite well (qualitatively). For a quantitative evaluation, the adhesion forces have to be known in order to estimate F_C. Unfortunately, they have not been determined experimentally in this case.

6 Conclusions and Outlook

In the beginning of this work, several numerical method to simulate the Tomlinson-mechanism were presented. The simple but quite powerful Tomlinson model allows to study the influence of cantilever actuation and thermal effects in both one and two dimensions. It could be shown for one dimension, that the temperature acts in a similar way than an actuated cantilever, meaning that 100 K higher temperature has the same effect on the average friction than an actuation of $\approx$0.1 "α". An analytical expression linking friction force, temperature and actuation should be developed in the future in order to compare with the simulations. Although this model still has the capabilities to be extended (e.g. by more springs), it seems to be clear that the future of friction simulation is applying atomistic simulation methods.

Finally, we have seen that contact AFM offers much more possibilities than simply scanning the topography. To obtain fundamental understanding of the tip-sample interaction, the analysis of contact resonances and stiffness is inevitable. The application of the dynamic superlubricity regime by actuation of the tip allowed us to reduce friction and thus scanning on a damageable system, NaCl on Cu(111). In order to track the contact resonance frequency, a novel AFM technique has applied, where a PLL is used to lock on the contact resonance frequency while scanning. This method allows to map the contact stiffness very fast, compared to grid-measurements. The fact that two different materials where accessible on the same sample allowed us to measure and compare these quantities. It could be shown (due to similar tip conditions), that (both) contact stiffness are about 20 % higher on Cu(111) than on NaCl. One important result is the fact that the normal contact stiffness seems to be about one order of magnitude larger than the lateral stiffness, thus resulting in a contact region involving approximately 5 atoms.

In order to obtain a better understanding of the contact dynamics, also higher normal (and torsional) resonances should be recorded, allowing to minimize the error in the normal contact stiffness. Thin alkali-halide films on metal are a good system to improve the technique of tracking the resonance frequency while scanning, since the two materials gives a high contrast.

7 Acknowledgments

At this point I would like to thank all the people that assisted me during the 6 month I spent here in the group of Prof. E. Meyer. The biggest thank goes to Dr. Thilo Glatzel, who never refused to help me when I was unable to solve the problem by my own and helped me writing and correcting the thesis. I would also like to thank Dr. Enrico Gnecco and Prof. Alexis Baratoff, who helped me especially with the theoretical issues and interpretation of the experiments. Last but not least I would thank Prof. Ernst Meyer who let me work at his group for this masterthesis and also for the fruitful talks I with him.

A Appendix

A.1 Q-Factor Determination

The quality factor or Q-factor is a dimensionless parameter that compares the time constant for decay (damping) of an oscillating physical system's amplitude to its oscillation period. So, a higher Q-factor corresponds to a system with less energy dissipation. In UHV, this energy loss is dominated by intrinsic friction of the silicon beam. There are mainly three techniques to determine Q-factors of cantilevers:

Frequency Sweep
By sweeping the frequency of excitation (frequency sweep), a characteristic resonance curve is produced. As a first approximation, the Q-factor $\approx f_0/\Delta f$, where Δf is the width of the resonance curve. But it is more precisely to fit the formulae for the driven harmonic oscillator for the amplitude $A(\omega)$ or the phase $\Phi(\omega)$. However, for soft contact cantilevers in UHV, this method is not very efficient, since one has to sweep very slowly.

Thermal Noise
It is possible to measure the Q-factor without excitation, just by fitting the PSD with eq. (4.3Cantilever Description and Propertiesequation.4.3). It has to be taken into account that the PSD produced by the Labview program "powerspectrum.vi" has to be recalibrated in order to get reasonable results. First, the Labview-data (in Watts) has to be divided with the bandwidth (e.g. 10 MHz). Then, after taken the square root and then multiplying with the sensitivity of the setup, one obtains the PSD in the common units $m/\sqrt{Hz}$. In this form, the data can be fitted with $\sqrt{S(\omega)}$.

Ring Down
Another method is to excite the cantilever and then suddenly switch off the excitation. By fitting the cantilevers amplitude, which should decay exponentially, the Q-factor can be determined easily. Here, the Q-factor can be understood as the number of oscillations before the amplitude dropped under 1/e of its initial value.

With all these method (which should be consistent) it is possible to obtain the Q-value for a free cantilever. Typically, Q$\approx$ 25000 for nc-levers and Q$\approx$ 400000 for contact levers.

A.2 Poisson's Ratio

When a sample of material is stretched in one direction, it tends to contract in the other two directions. Poisson's ratio ν, named after Simeon Poisson, is a measure of this tendency. Poisson's ratio is the ratio of the relative contraction strain τ_{con}

(normal to the applied load), divided by the relative extension strain τ_{ext} (in the direction of the applied load):

$$\nu = -\frac{\tau_{con}}{\tau_{ext}} \quad . \tag{A.1}$$

A.3 Generation of Gaussian Random Numbers

In physical phenomena, stochastic variables such as velocity distribution (in each dimension) are often Gaussian distributed. Since most numerical pseudo random number generators produce uniform distributed numbers, they must be transformed. The probably most important of these transformation is the Box-Muller transformation [75]. The most basic form of this transformation looks like

$$\begin{aligned} y_1 &= \sqrt{-2log(x_1)}cos(2\pi x_2) \quad , \quad and \\ y_2 &= \sqrt{-2log(x_1)}sin(2\pi x_2) \quad , \end{aligned} \tag{A.2}$$

where x_1 and x_2 are uncorrelated uniform distributed random numbers in the range from 0 to 1). After this transformation, we end up with two correlated, Gaussian distributed random numbers y_1 and y_2, which are used as thermal noise for the Ermak's algorithm.

A.4 Terms B_1, B_2, B_3

$$\begin{aligned} B_1 &= \left(\frac{h}{L_1}\right)^2 (k_n L_1)^3 \left(sin^2\epsilon + \frac{\kappa}{k^*}cos^2\epsilon\right) \\ &\times [(1 + cosk_nL'coshk_nL')(sink_nL_1coshk_nL1 \\ &+ cosk_nL_1sinhk_nL_1) - (1 - cosk_nL_1coshk_nL_1) \\ &\times (sink_nL'coshk_nL' + cosk_nL'sinhk_nL')] \end{aligned}$$

$$\begin{aligned} B_2 &= \left(\frac{h}{L_1}\right) (k_n L_1)^2 \left(\left(\frac{\kappa}{k^*}\right) sin\epsilon + cos\epsilon\right) \\ &\times [(1 + cosk_nL'coshk_nL')sink_nL_1sinhk_nL_1 \\ &+ (1 - cosk_nL_1coshk_nL_1)sink_nL'sinhk_nL'] \end{aligned}$$

$$\begin{aligned} B_3 &= (k_n L_1) \left(cos^2\epsilon + \frac{\kappa}{k^*}sin^2\epsilon\right) \\ &\times [(1 + cosk_nL'coshk_nL')(sink_nL_1coshk_nL1 \\ &- cosk_nL_1sinhk_nL_1) - (1 - cosk_nL_1coshk_nL_1) \\ &\times (sink_nL'coshk_nL' - cosk_nL'sinhk_nL')] \end{aligned}$$

A.5 List of Used Open-Source Software

Here a list of the software that has been used after the data acquisition with Nanonis SPM Software. All of these programs are open-source, so they are non-commercial. A big thank to the programmers of these great tools!

Operating Systems
Ubuntu 7.10
Fedora 8

SPM Image Analysis
Gwyddion 2.9.3

General Image Processing
GIMP 2.4.2
OpenOffice Drawing 2.3

Data Handling and Organization
Gnumeric 1.7.11

Data Plotting and Fitting
Gnuplot 4.2
Grace 5.1.21

Algebraic Calculator
Maxima 5.12.0

Numeric Calculator
Octave 2.9

Text Processing and Presentations
gedit 2.22.1
VIM 7.1.138
OpenOffice Writer 2.3
OpenOffice Presentation 2.3
Tex Live

Fortran Compiler
Gfortran 4.2.1

Reference Manager
Jabref 2.2

References

[1] Y.Z. Hu and S. Granick. Microscopic study of thin film lubrication and its contributions to macroscopic tribology. *Tribology Letters*, 5:8188, 1998.

[2] A. Socoliuc, E. Gnecco, S. Maier, O. Pfeiffer, A. Baratoff, R. Bennewitz, and E. Meyer. Atomic-scale control of friction by actuation of nanometer-sized contacts. *Science*, 313(5784):207–210, 2006.

[3] G. Binnig, C.F. Quate, and Ch. Gerber. Atomic force microscope. *Physical Review Letters*, 56(9):930–933, 1986.

[4] http://en.wikipedia.org/wiki/afm, 2006.

[5] G. Meyer and N.M. Amer. Novel optical approach to atomic force microscopy. *Applied Physics Letters*, 53(12):1045–1047, 1988.

[6] F.J. Giessibl. Advances in atomic force microscopy. *Reviews of Modern Physics*, 75(3):949–983, 2003.

[7] Y. Martin, C.C. Williams, and H.K. Wickramasinghe. Atomic force microscope–force mapping and profiling on a sub 100 Å scale. *Journal of Applied Physics*, 61(10):4723–4729, 1987.

[8] T.R. Albrecht, P. Grutter, D. Horne, and D. Rugar. Frequency modulation detection using high-q cantilevers for enhanced force microscope sensitivity. *Journal of Applied Physics*, 69(2):668–673, 1991.

[9] F.J. Giessibl. Forces and frequency shifts in atomic-resolution dynamic-force microscopy. *Physical Review B*, 56(24):16010–16015, 1997.

[10] E. Meyer, H.J. Hug, and R. Bennewitz. *Scanning Probe Microscopy*. Springer, 2003.

[11] Q. Zhong, D. Inniss, K. Kjoller, and V. B. Elings. Fractured polymer/silica fiber surface studied by tapping mode atomic force microscopy. *Surface Science*, 290(1-2):L688–L692, 1993.

[12] M. Nonnenmacher, M.P. O'Boyle, and H.K. Wickramasinghe. Kelvin probe force microscopy. *Applied Physics Letters*, 58(25):2921–2923, 1991.

[13] Y. Martin and H.K. Wickramasinghe. Magnetic imaging by "force microscopy" with 1000 Å resolution. *Applied Physics Letters*, 50(20):1455–1457, 1987.

[14] U. Rabe, S. Amelio, E. Kester, V. Scherer, S. Hirsekorn, and W. Arnold. Quantitative determination of contact stiffness using atomic force acoustic microscopy. *Ultrasonics*, 38(1-8):430–437, 2000.

[15] F.P. Bowden and D. Tabor. The friction and lubrication of solids. *Oxford University Press*, (2938):337, 1950.

[16] H. Hertz. Über die Berührung fester elastischer Körper. *Journal für die reine und angewandte Mathematik*, 92:156, 1881.

[17] J.F. Archard. Elastic deformation and the laws of friction. *Proceedings of the Royal Society of London. Series A, Mathematical and Physical Sciences*, 243(1233):190–205, 1957.

[18] A. Volmer and T. Nattermann. Towards a statistical theory of solid dry friction. *Zeitschrift fr Physik B*, 104:363, 1997.

[19] J.A. Greenwood and J. B. P. Williamson. Contact of nominally flat surfaces. *Proceedings of the Royal Society of London*, 295:300, 1966.

[20] E. Meyer, R.M. Overney, K. Dransfeld, and T. Gyalog. *Nanoscience - Friction and Rheology on the Nanometer Scale*. World Scientific, 1998.

[21] M.C. Mate, G.M. McClelland, R. Erlandsson, and S. Chiang. Atomic-scale friction of a tungsten tip on a graphite surface. *Physical Review Letters*, 59(17):1942–1945, 1987.

[22] G.A. Tomlinson. A molecular theory of friction. *Philosophical Magazine*, 7:905, 1929.

[23] A. Socoliuc, R. Bennewitz, E. Gnecco, and E. Meyer. Transition from stick-slip to continuous sliding in atomic friction: Entering a new regime of ultralow friction. *Physical Review Letters*, 92(13):134301, 2004.

[24] S. Maier. *Contact Dynamics from the Atomic Scale to Nanostructured Surfaces*. PhD thesis, University of Basel, 2006.

[25] S. Maier, E. Gnecco, A. Baratoff, R. Bennewitz, and E. Meyer. Atomic-scale friction modulated by a buried interface. *to be published*.

[26] P. Langevin. Sur la théorie de mouvement brownien. *Les Comptes rendus de l'Académie des sciences*, 146:530, 1908.

[27] P. Reimann and M. Evstigneev. Description of atomic friction as forced brownian motion. *New Journal of Physics*, 7:25, 2005.

[28] R. Bennewitz, E. Gnecco, T. Gyalog, and E. Meyer. Atomic friction studies on well-defined surfaces. *Tribology Letters*, 10:51, 2001.

[29] J. L. Lubkin. *Handbook of Engineering Mechanics*. McGraw-Hill, 1962.

[30] K. L. Johnson. *Contact Mechanics*. Cambridge University Press, 1985.

[31] U. Rabe. *Applied Scanning Probe Methods II, Chapter 2.* Springer Berlin Heidelberg, 2006.

[32] D.C. Hurley and J.A. Turner. Measurement of Poisson's ratio with contact-resonance atomic force microscopy. *Journal of Applied Physics*, 102(3):033509, 2007.

[33] M. Reinstadtler, T. Kasa, U. Rabe, B. Bhushan, and W. Arnold. Imaging and measurement of elasticity and friction using the TRmode. *Journal of Physics D*, 38(18):R269–R282, 2005.

[34] C.S. Hodges, L. Looi, J.A.S. Cleaver, and M. Ghadiri. Use of the JKR model for calculating adhesion between rough surfaces. *Langmuir*, 20(22):9571–9576, 2004.

[35] B.V. Derjaguin, V.M. Muller, and Y.P. Toporov. Effect of contact deformations on the adhesion of particles. *Journal of Colloid and Interface Science*, 53(2):314–326, 1975.

[36] B. Luan and M.O. Robbins. The breakdown of continuum models for mechanical contacts. *Nature*, 435(7044):929–932, 2005.

[37] B. Luan and M.O. Robbins. Contact of single asperities with varying adhesion: Comparing continuum mechanics to atomistic simulations. *Physical Review E*, 74(2):026111, 2006.

[38] M.P. Allen and D.J. Tildesley. *Computer Simulations of Liquids.* Oxford Univeristy Press, 1991.

[39] T. Gyalog, M. Bammerlin, R. Lüthi, E. Meyer, and H. Thomas. Mechanism of atomic friction. *Europhysics Letters*, 31(5-6):269–274, 1995.

[40] E. Gnecco, R. Bennewitz, T. Gyalog, Ch. Loppacher, M. Bammerlin, E. Meyer, and H.-J. Güntherodt. Velocity dependence of atomic friction. *Physical Review Letters*, 84:1172, 2000.

[41] Y. Sang, M. Dub, and M. Grant. Thermal effects on atomic friction. *Physical Review B*, 87:174301, 2001.

[42] Y. Sang, M. Dube, and M. Grant. Dependence of friction on roughness, velocity, and temperature. *Physical Review E*, 77(3):036123, 2008.

[43] M. Evstigneev and P. Reimann. Rate description of the stick-slip motion in friction force microscopy experiments. *Physical Review E*, 71(5):056119–8, 2005.

[44] A. Baratoff. private communication.

[45] G.S. Verhoeven, M. Dienwiebel, and J.W.M. Frenken. Model calculations of superlubricity of graphite. *Physical Review B*, 92:126101, 2004.

[46] A. Ghasemi. private communication.

[47] L. Zimmerli. *Assemblies of Organic Molecules on Insulating Surfaces Investigated by nc-AFM*. PhD thesis, University of Basel, 2007.

[48] L. Howald, E. Meyer, R. Lüthi, H. Haefke, R. Overney, H. Rudin, and H.-J. Güntherodt. Multifunctional probe microscope for facile operation in ultrahigh vacuum. *Applied Physics Letters*, 63(1):117–119, 1993.

[49] NANONIS. http://www.nanonis.com.

[50] J.P. Cleveland, S. Manne, D. Bocek, and P.K. Hansma. A nondestructive method for determining the spring constant of cantilevers for scanning force microscopy. *Review of Scientific Instruments*, 64(2):403–405, 1993.

[51] J.E. Sader, I. Larson, P. Mulvaney, and L.R. White. Method for the calibration of atomic force microscope cantilevers. *Review of Scientific Instruments*, 66(7):3789–3798, 1995.

[52] L.D. Landau and E.M. Lifshitz. *Theroy of Elasticity*. Elsevier, 1986.

[53] S. Rast, C. Wattinger, U. Gysin, and E. Meyer. The noise of cantilevers. *Nanotechnology*, 11(3):169–172, 2000.

[54] R.J. Cannara, M. Eglin, and R.W. Carpick. Lateral force calibration in atomic force microscopy: A new lateral force calibration method and general guidelines for optimization. *Review of Scientific Instruments*, 77(5):053701, 2006.

[55] U.D. Schwarz, P. Koster, and R. Wiesendanger. Quantitative analysis of lateral force microscopy experiments. *Review of Scientific Instruments*, 67(7):2560–2567, 1996.

[56] A. Socoliuc. *Control of friction on the atomic scale*. PhD thesis, University of Basel, 2005.

[57] G. Matei, S. Jeffery, S. Patil, S.H. Khan, M. Pantea, J.B. Pethica, and P.M. Hoffmann. Simultaneous normal and shear measurements of nanoconfined liquids in a fiber-based atomic force microscope. *Review of Scientific Instruments*, 79(2):023706, 2008.

[58] R. Bennewitz, V. Barwich, M. Bammerlin, C. Loppacher, M. Guggisberg, A. Baratoff, E. Meyer, and H. J. Güntherodt. Ultrathin films of NaCl on Cu(111): A LEED and dynamic force microscopy study. *Surface Science*, 438(1-3):289–296, 1999.

[59] R. Bennewitz, A.S. Foster, N. L.Kantorovich, M. Bammerlin, Chr. Loppacher, S. Schr, M. Guggisberg, E. Meyer, and A.L. Shluger. Atomically resolved edges and kinks of NaCl islands on Cu(111): Experiment and theory. *Physical Review B*, 62(3):2074–2084, 2000.

[60] L. Romanioni. *Adsorption and self-organization of CuOEP on heterogeneous surfaces:tuning the molecule-substrate interaction.* PhD thesis, University of Basel, 2005.

[61] T. Filleter, W. Paul, and R. Bennewitz. Atomic structure and friction of ultrathin films of KBr on Cu(100). *Physical Review B*, 77(3):035430, 2008.

[62] E. Gnecco, A. Socoliuc, S. Maier, J. Gessler, T. Glatzel, A. Baratoff, and E. Meyer. Dynamic superlubricity on insulating and conductive surfaces in ultra-high vacuum and ambient environment. *to be published.*

[63] T. Glatzel and L. Zimmerli. private communication.

[64] S.Yu. Krylov, J.A. Dijksman, W.A. van Loo, and J.W.M. Frenken. Stick-slip motion in spite of a slippery contact: Do we get what we see in atomic friction? *Physical Review Letters*, 97(16):166103, 2006.

[65] E. Gnecco, R. Bennewitz, T. Gyalog, and E. Meyer. Friction experiments on the nanometre scale. *Journal of Physics: Condensed Matter*, 13(31):R619–R642, 2001.

[66] M.A. Lantz, S.J. O'Shea, A.C.F. Hoole, and M.E. Welland. Lateral stiffness of the tip and tip-sample contact in frictional force microscopy. *Applied Physics Letters*, 70(8):970–972, 1997.

[67] S. Maier, O. Pfeiffer, T. Glatzel, E. Meyer, T. Filleter, and R. Bennewitz. Asymmetry in the reciprocal epitaxy of NaCl and KBr. *Physical Review B*, 75(19):195408, 2007.

[68] J.A. Turner. Non-linear vibrations of a beam with cantilever-hertzian contact boundary conditions. *Journal of Sound and Vibration*, 275(1-2):177–191, 2004.

[69] K. Grudziski and R. Kostek. An analysis of nonlinear normal contact microvibrations excited by a harmonic force. *Nonlinear Dynamics*, 50:809, 2007.

[70] J.A. Turner, S. Hirsekorn, U. Rabe, and W. Arnold. High-frequency response of atomic-force microscope cantilevers. *Journal of Applied Physics*, 82(3):966–979, 1997.

[71] U. Rabe, K. Janser, and W. Arnold. Vibrations of free and surface-coupled atomic force microscope cantilevers: Theory and experiment. *Review of Scientific Instruments*, 67(9):3281–3293, 1996.

[72] U. Rabe, J.A. Turner, and W. Arnold. Analysis of the high-frequency response of atomic force microscope cantilevers. *Applied Physics A*, 66(0):S277–S282, 1998.

[73] R.W. Stark and W.M. Heckl. Higher harmonics imaging in tapping-mode atomic-force microscopy. *Review of Scientific Instruments*, 74(12):5111–5114, 2003.

[74] D. Rupp, U. Rabe, S. Hirsekorn, and W. Arnold. Nonlinear contact resonance spectroscopy in atomic force microscopy. *Journal of Physics D*, 40(22):7136–7145, 2007.

[75] G.E.P. Box and M.E. Muller. A note on the generation of random normal deviates. *Annals of Mathematical Statistics*, 29:610, 1958.